



Roughness-Induced Instabilities and Transition on a Generic Hypersonic Forebody at Mach 6

Julien Lefieux* and Eric Garnier†

Université Paris Saclay, F-92190, Meudon, France

Jean-Philippe Brazier‡

Université de Toulouse, F-31055 Toulouse, France

Neil D. Sandham§

University of Southampton, Southampton, England SO17 1BJ, United Kingdom

and

Antoine Durant¶

MBDA-France, 92350 Le Plessis-Robinson, France

<https://doi.org/10.2514/1.J059972>

In hypersonic flows, it is often necessary to be able to trip the transition to turbulence, upstream of air intakes, for example. Direct numerical simulations have been performed to identify the roughness-induced transition mechanisms on a wedgelike forebody at Mach 6 and unit Reynolds number $Re = 11$ million (/m). Good agreement with the experiments performed in the Boeing/Air Force Office of Scientific Research Mach-6 Quiet Tunnel at Purdue University was obtained in terms of wall heat-flux and wall-pressure fluctuations. First, an isolated roughness was considered. The presence of the roughness in the span-inhomogeneous base flow leads to the formation of a crossflowlike vortex. High-frequency secondary instabilities of the stationary crossflow vortex are observed in the wake and are found to be responsible for the breakdown to turbulence. Spatial linear modal instability analysis of this flow has been performed at selected streamwise locations. The linear stability approach is found to give accurate predictions in terms of mode shapes, most-amplified disturbance frequencies, and growth rates, as it only underpredicts the N-factor of the most unstable mode by 10% compared to the direct numerical simulations. Unsteady simulations were then carried out for a trip array configuration and showed that it does not change the transition mechanisms, but the frequencies of the most unstable secondary instabilities were found to be higher.

Nomenclature

C_f	= skin-friction coefficient
D	= roughness width, mm
E	= total energy, $\text{m}^2 \cdot \text{s}^{-2}$
f	= frequency, Hz
k	= roughness height, mm
L	= length, m
M	= Mach number
N	= number of grid points
N_f	= N-factor
P	= pressure, Pa
Pr	= Prandtl number
Q	= second invariant of the velocity gradient tensor
q_j	= heat-flux vector, W/m^2
R	= universal gas constant
Re	= freestream unit Reynolds number, m^{-1}
S^*	= Sutherland's reference temperature, K
s	= spacing between roughness elements center to center, mm
T	= temperature, K
t	= time, s

u, v, w	= streamwise, spanwise, and vertical velocities, $\text{m} \cdot \text{s}^{-1}$
x, y, z	= Cartesian coordinates, m
α	= streamwise wave number
β	= spanwise wave number
γ	= ratio of specific heats
δ	= 99% boundary-layer thickness, m
δ_{ij}	= Kronecker delta function
λ	= thermal conductivity, $\text{W} \cdot \text{m}^{-1} \cdot \text{K}^{-1}$
μ	= dynamic viscosity $\text{kg} \cdot \text{m}^{-1} \cdot \text{s}^{-1}$
ρ	= density $\text{kg} \cdot \text{m}^{-3}$
τ_{ij}	= viscous stress tensor
ω	= angular frequency

Subscripts

i	= imaginary part
k	= value at roughness location
r	= real part
w	= value at the wall
∞	= freestream value

Superscripts

$/$	= fluctuating quantity
$*$	= reference value

I. Introduction

UNDERSTANDING and predicting the effect of roughness on the laminar-turbulent transition in hypersonic boundary layers [1] are crucial for the design of hypersonic flight vehicles. As mentioned by [2], most current scramjet vehicles have a planar (nonaxisymmetric) flowpath for better propulsion performance. The weak growth factor of natural instabilities makes it difficult for the flow to go through the transition to turbulence. Shock-wave interactions with laminar boundary layers are likely to create separation upstream of the engine intakes, thus decreasing the flight performance of

Received 8 July 2020; revision received 29 January 2021; accepted for publication 7 February 2021; published online 31 May 2021. Copyright © 2021 by the American Institute of Aeronautics and Astronautics, Inc. All rights reserved. All requests for copying and permission to reprint should be submitted to CCC at www.copyright.com; employ the eISSN 1533-385X to initiate your request. See also AIAA Rights and Permissions www.aiaa.org/randp.

*Ph.D. Candidate, Aerodynamics, Aeroelasticity, Acoustics Department (DAAA), ONERA; julien.lefieux@onera.fr.

†Senior Scientist, Research Engineer, Aerodynamics, Aeroelasticity, Acoustics Department (DAAA), ONERA; eric.garnier@onera.fr.

‡Senior Scientist, Research Engineer, DMPE, ONERA.

§Professor, Faculty of Engineering and the Environment. Senior Member AIAA.

¶Engineer, Aerodynamics & Performance, 1 Avenue Réaumur.

airbreathing vehicles. Roughness elements may be used to act as a source of disturbance for a developing laminar boundary layer to trigger the transition to turbulence upstream of the engine intakes. The understanding of transition mechanisms induced by roughness elements in hypersonic flows remains limited to relatively simple configurations such as flat plates, axisymmetric cones, or elliptic cones. The purpose of the present work is to study the effects of roughness elements on the laminar-turbulent transition in the three-dimensional boundary layer of a complex hypersonic forebody.

The natural instabilities likely to grow in the boundary layer of hypersonic forebodies are relatively well-known. Bartkowicz et al. [3] focused on the natural transition on an elliptic cone and showed the importance of stationary crossflow vortices giving birth to longitudinal streaks, which can in turn induce secondary instabilities when the Reynolds number is increased. Paredes et al. [4] revealed four types of linear instabilities on the Hypersonic International Flight Research Experimentation-5 geometry: symmetric and antisymmetric centerline instabilities, attachment-line instabilities, and crossflow and oblique second-mode instabilities. Experiments have been carried out on a yawed circular cone and showed the importance of secondary instabilities of the stationary crossflow vortex in the three-dimensional boundary layer of the forebody [5,6]. This was verified in the secondary instability analysis performed by Moyes et al., which also showed high-frequency second modes that coexist with the shear-layer instabilities [7] as well as the existence of low-frequency traveling crossflow modes [8,9].

Recent studies have focused on the instabilities induced by a diamond-shaped roughness element on a flat plate boundary layer. Direct numerical simulations from Shrestha and Candler [10] revealed the source of instability to be an interaction between the shear layers and the counter-rotating streamwise vortices. The use of a trip array instead of an isolated roughness did not change the dominant mode of instability, but its peak-amplitude frequency was higher, and the transition onset location moved further upstream. Stability analysis from Choudhari et al. [11] showed the existence of even (i.e., symmetric or varicose) and odd (antisymmetric or sinuous) modes of instability in the wake of the roughness.

The effect of roughness on the hypersonic boundary layer over more realistic configurations has been numerically studied. The transition mechanisms induced by singular and distributed roughnesses over a capsulelike hemispherical forebody were investigated via direct numerical simulations (DNS) and linear stability analyses (LST) [12]. Results showed the presence of two main unstable modes (symmetric and antisymmetric modes) in the singular roughness wake. A crossflowlike vortex was generated when using a patch of pseudorandomly distributed roughness and was found to be subject to secondary instabilities of the crossflow vortex. Among a number of works concerning transition on forebodies (e.g., [13,14]), computations of secondary instability of crossflow modes in the hypersonic boundary layer over a circular cone excited by azimuthally periodic roughness were carried out by Li et al. [15]. They showed that the second-mode (i.e., Mack mode) instabilities were the most unstable high-frequency disturbances, along with secondary instabilities of the finite-amplitude stationary crossflow vortices. Low-frequency modes were also found and identified as traveling crossflow instabilities. DNS and two-dimensional LST (LST-2D) computations investigated the dominant instabilities induced by an azimuthally periodic and a localized roughness. The frequencies of the most-amplified secondary disturbances were found to be in the range of 200 to 360 kHz [11]. These configurations were also analyzed with Parabolized Stability Equations (PSE) computations in both linear and nonlinear stages [16]. Results showed the ability of the quasi-parallel stability analysis to predict the general topology of the instability modes and their associated dominant frequencies. However, it severely underpredicted the N-factors for the dominant instability modes. The PSE results were found to give predictions in agreement with the DNS results extending across mode shapes, dominant frequencies, and N-factors.

Experiments were carried out by Durant et al. [17] in the Boeing/U.S. Air Force Office of Scientific Research Mach 6 Quiet Tunnel (BAM6QT) at Purdue University to study roughness-induced transition

on a generic hypersonic forebody. The boundary layer on the wedgelike forebody model was tripped either by isolated or distributed diamond-shaped roughness elements of different heights. Temperature-sensitive paint (TSP) enabled heat fluxes on the surface of the forebody to be quantified. PCB sensors were also used to measure fluctuations in the surface pressure. On the same geometry, computational studies can be found in the works of Orlik et al. [18], who showed the existence of traveling crossflow instability and oblique first-mode instability; André et al. [19], who focused on active flow tripping by wall injection; and Cerminara et al. [20], who investigated the receptivity and breakdown mechanisms with freestream acoustic disturbance.

Advances in numerical methods and computing capabilities now make it possible to study complex configurations of roughness-induced transition in hypersonic flows with a good accuracy. In the present work, direct numerical simulations have been performed to reproduce this experiment. This aims at gaining some physical understanding of the transition mechanisms induced by a roughness immersed in a span-inhomogeneous base flow, that is, whose boundary layer thickness is not constant over the span of the forebody, that includes a streamwise vortex. For that purpose, validating the LST approach against the DNS data is of great interest.

The paper is organized as follows. First, the computational setup is presented (Sec. II). Then the unsteady simulation results are validated against the experimental data (Sec. III). LST-2D analysis is first performed on the smooth geometry (Sec. IV). DNS and stability results are then analyzed to get insight into the transition mechanisms induced by an isolated roughness element (Sec. V). Finally, the effect of adding a row of roughness is investigated via direct numerical simulations (Sec. VI).

II. Configurations and Numerical Setup

A. Reference Experiment

Transition experiments involving passive roughness elements and active wall injection were conducted in the BAM6QT at Purdue University [17]. The wedgelike forebody model used in these experiments is shown in Fig. 1. It was 0.34 m long. It was covered with TSP and was equipped with Schmidt–Boelter sensors for heat-flux measurements and with PCB sensors to analyze wall-pressure fluctuations downstream of the roughness elements.

The flow is set to Mach 6, at a Reynolds number of 11×10^6 (/m) and the forebody is set to an angle of attack of 4 deg. During each run of the wind-tunnel tests, the stagnation pressure decreases, and so does the Reynolds number. The freestream temperature and pressure are $T_\infty = 51.7$ K and $P_\infty = 629.6$ Pa, respectively. Among the configurations experimentally tested, only two cases were retained in the present work involving an isolated roughness element of height 0.8 mm (case I8), and a row of roughness of height 0.8 mm (R8). Note that the full-span forebody was tested in the experiment. The isolated diamond-shaped roughness elements (I8) are placed at $x_k = 0.100$ m and $y_k = -0.018$ m on the windward surface of the forebody. In the

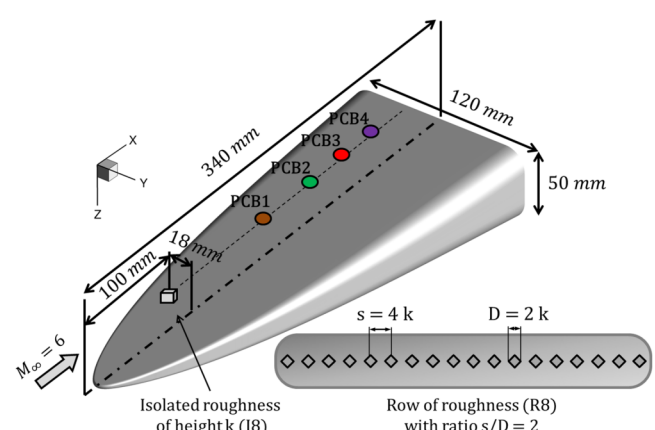


Fig. 1 Generic hypersonic forebody model used in BAM6QT experiments.

case of the roughness array (R8), in the experiment, 18 diamond-shaped roughness elements were placed at $x_k = 0.100$ m. The computations take advantage of the symmetry of the forebody and nine diamond-shaped roughness elements are used, on the half-span forebody for $y < 0$. Roughness elements scale only with the parameter k , the roughness height. Viewed from its top, a single roughness element diagonal length is $D = 2k$. The distance between two successive roughness centers is $s = 4k$, which results in a trip-spacing ratio of $s/D = 2$.

Both cases were successful in triggering transition before the end of the forebody. For each case, the roughness parameters, such as the ratio of roughness height to boundary-layer thickness and the roughness Reynolds number, are summarized in Table 1. The roughness Reynolds number is defined as $Re_{kk} = \rho_k u_k k / \mu(T_k)$ [21]. The values of k/δ and Re_{kk} for each roughness element of the R8 configuration are shown in Fig. 2. Mach number contours of the base flow induced by the smooth forebody at streamwise location $x = 0.100$ m are also shown to highlight the spanwise inhomogeneity of the boundary layer.

B. Numerical Setup

In this work, the full compressible Navier–Stokes equations are solved for a Newtonian fluid with viscosity μ :

$$\begin{aligned} \frac{\partial \rho}{\partial t} + \frac{\partial \rho u_j}{\partial x_j} &= 0 \\ \frac{\partial \rho u_i}{\partial t} + \frac{\partial \rho u_i u_j}{\partial x_j} + \frac{\partial p}{\partial x_i} &= \frac{\partial \tau_{ij}}{\partial x_j} \\ \frac{\partial \rho E}{\partial t} + \frac{\partial (\rho E + p) u_i}{\partial x_i} &= -\frac{\partial q_i}{\partial x_i} + \frac{\partial u_i \tau_{ij}}{\partial x_j} \end{aligned} \quad (1)$$

where ρ is the density and u_i is the velocity component in the i -coordinate direction ($i = 1, 2, 3$); $E = p/(\rho(\gamma - 1)) + u_i u_i / 2$ is the total energy per unit mass. The symmetric viscous stress tensor τ_{ij} is defined as

$$\tau_{ij} = \frac{\mu}{Re} \left(\frac{\partial u_j}{\partial x_i} + \frac{\partial u_i}{\partial x_j} - \frac{2}{3} \frac{\partial u_k}{\partial x_k} \delta_{ij} \right) \quad (2)$$

where δ_{ij} is the Kronecker delta function defined as $\delta_{ij} = 1$ for $i = j$ and $\delta_{ij} = 0$ for $i \neq j$. The equation of state for a perfect gas is considered for the calculations of the fluid properties. Fourier's law of heat conduction is used for the heat-flux vector q_j :

Table 1 Roughness parameters used for the simulated cases

Case	k , mm	k/δ	Re_{kk}
I8	0.8	0.8	1232
R8	0.8	[0.23, 1.02]	[183, 6200]

The values in brackets represent the minimum and maximum values obtained with the row of roughness R8.

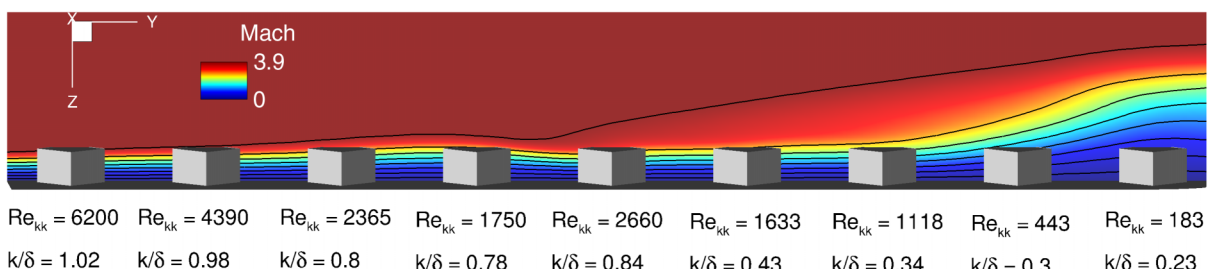


Fig. 2 Roughness parameters for the row of roughness R8 along with Mach number contours of the smooth forebody base flow at $x = 0.100$ m.

$$q_j = -\frac{\mu}{(\gamma - 1) M_\infty^2 Pr Re} \frac{\partial T}{\partial x_j} \quad (3)$$

The molecular viscosity is computed using Sutherland's law:

$$\mu(T) = \mu_0 \left(\frac{T}{T_0} \right)^{\frac{3}{2}} \frac{T_0 + S^*}{T + S^*} \quad (4)$$

where $S^* = 110.4$ K is the Sutherland reference temperature, $\mu_0 = 1.711 \times 10^{-5}$ kg/(m · s), and $T_0 = 273$ K.

The compressible Navier–Stokes equations were numerically solved on a structured mesh using the in-house finite-volume solver elsA [22]. The second-order AUSM+ scheme [23] was selected for spatial discretization, coupled with a third-order limiter. Previous validation against high-order schemes showed that the current spatial discretization was suitable for predicting the roughness-induced transitional flow on a flat plate at Mach 6 [24]. The diffusion flux densities are evaluated thanks to a five-point stencil centered discretization. Time integration is made using an implicit Gear method of second order, with 10 Gear subiterations in order to increase the time step and reduce the computational time. The time step is 2×10^{-8} s. The simulated physical time after cleaning out the transient state is 5 ms, which corresponds to around 15 flow-through domains.

For the computation of the laminar base flow used in the stability analysis, steady simulations were carried out with elsA. The reason a laminar base flow was successfully computed, whereas the final DNS were unsteady, was that the numerical method was adapted. A Roe scheme was used for the computation of the convective fluxes, along with a minmod limiter, more dissipative than the third-order limiter. Time integration is achieved using an implicit (backward Euler) scheme. The system was integrated in time at a CFL (Courant–Friedrichs–Lowy) number up to 60, until a decrease of four orders of magnitude in the average residual was achieved.

C. Chimera Method and Grid Convergence Study

The computational domain and boundary conditions are shown in Fig. 3. To reduce the computational cost, only half of the forebody is simulated and a symmetry boundary condition is applied in plane (O, x, z). A uniform supersonic flow is imposed at the inlet of the computational domain. The forebody and the roughness elements are assumed to be isothermal and set to the initial model temperature of $T_w = 300$ K. Experimental calibration obtained from Schmidt–Boelter heat transfer gauges revealed that this was a reasonable assumption. The initial model temperature recorded in the experiment was 301.3 K for the I8 case and 297.9 K in the R8 case.

The grid around the forebody is seen in Fig. 4. The boundaries of the computational domain were constructed so that the grid around the forebody is aligned with the leading-edge shock. This prevents numerical oscillations coming from a lack of grid resolution at the shock location.

In the experiments, laminar flow could be observed with the smooth insert with no roughness. To know the grid refinement needed for accurately predicting this laminar flow, steady laminar simulations were carried out, with a coarse grid of 50 million cells and a fine grid of 200 million cells. Figure 5 shows a comparison of velocity profiles at the roughness streamwise location for several spanwise locations on the smooth forebody. As seen on the spanwise velocity v

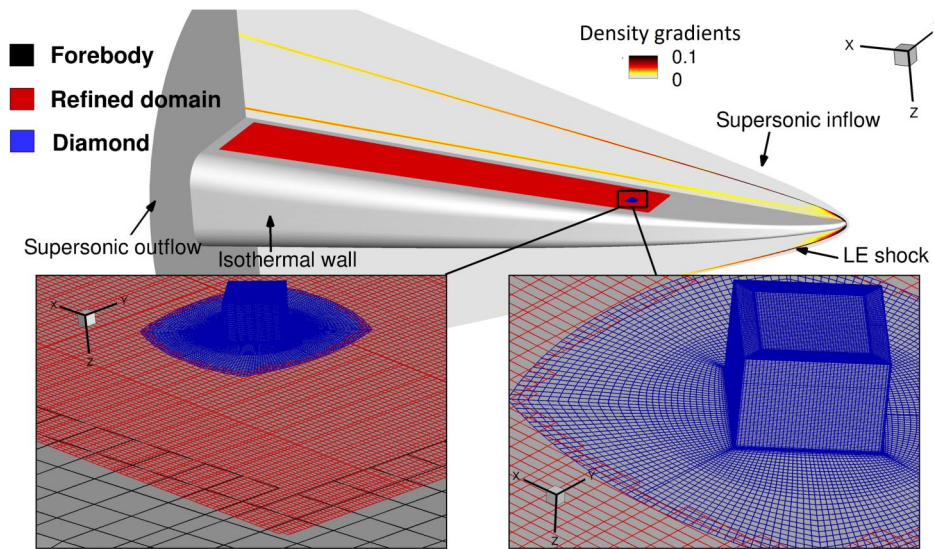


Fig. 3 Computational domain and boundary conditions. A Chimera grid system is used with three overlapping grids for an isolated roughness element I8 ($k = 0.8$ mm). The leading-edge shock is visualized with contours of density gradient magnitude in the symmetry plane.

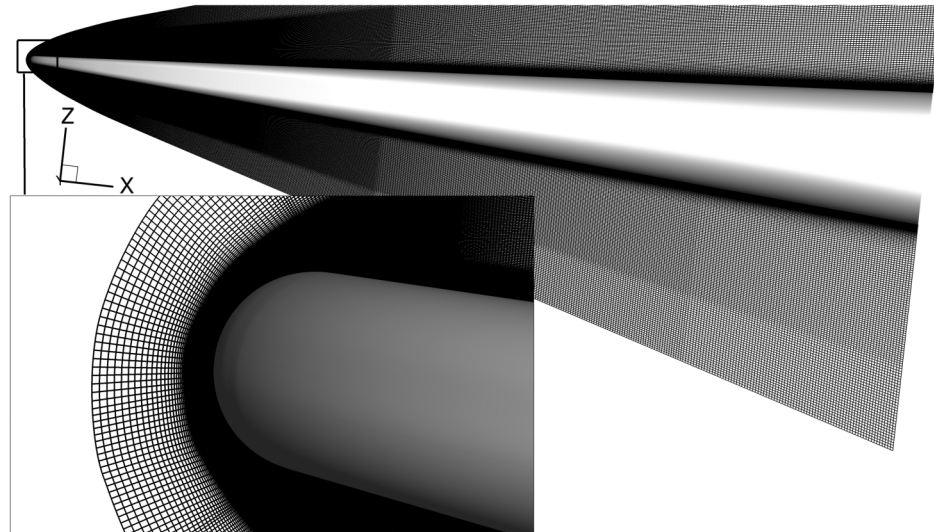


Fig. 4 Grid around the forebody shown in the symmetry plane. The computational domain follows the shape of the leading-edge shock so that the grid is aligned with the shock to prevent numerical oscillations.

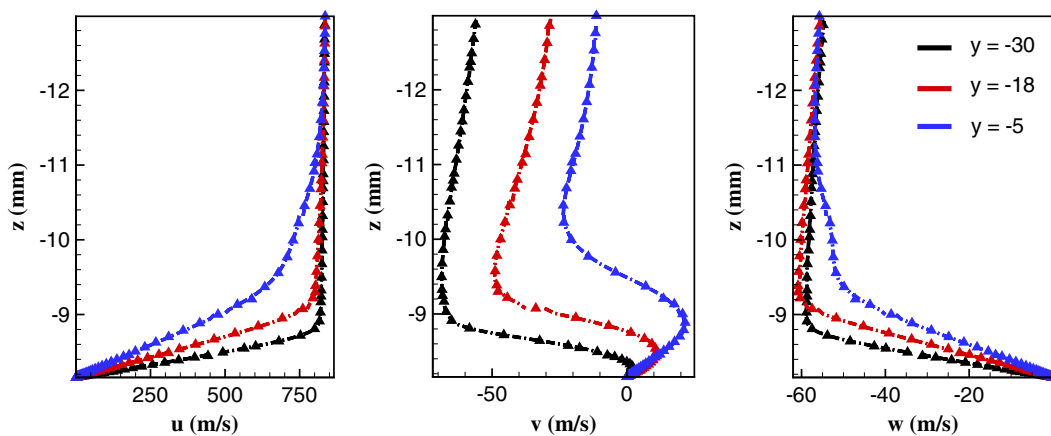


Fig. 5 Comparison of streamwise, spanwise, and vertical velocity profiles obtained with fine (line) and coarse (symbols) grids, containing 200 million and 50 million cells, respectively, for several spanwise locations at the roughness streamwise location $x = 0.100$ m.

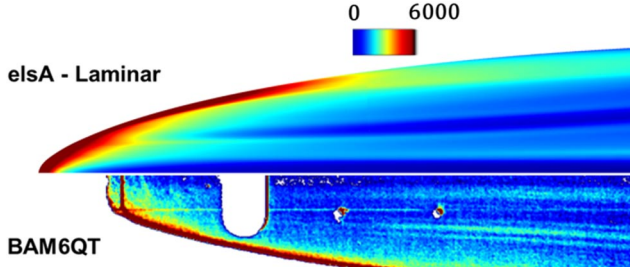


Fig. 6 Time-averaged wall heat flux in W/m^2 on the smooth forebody. Comparison with experiments.

profiles, there exists a spanwise component of the velocity that is caused by the motion of the fluid from the attachment line towards the symmetry plane. The coarse grid of 50 million cells is used for comparison with the experimental wall heat flux in Fig. 6 since it was found to give the same results as the 200 million-cell grid in terms of wall heat flux. The coarse grid is thus fine enough for computing a laminar base flow (with steady simulation) on the smooth geometry. Note that the nose of the experimental model was not covered with TSP. Hence, it does not appear in the postprocessed images of the wall heat flux. One can see that the wall heat-flux level is globally similar. Reasonable agreement is obtained in the region upstream of the smooth insert. Close to the centerline, the low heat flux is predicted as well as the low heat flux in the midspan region. The main difference can be seen in the fine thin stripes present in the measurements but not in the computation. These fine stripes would likely be obtained in a time-resolved DNS, with the addition of freestream disturbances, as it is supposed to be the case in the wind tunnel. However, the purpose of the present work is to study the transition mechanisms induced by roughness. The use of a refined domain with the Chimera method will allow the roughness wake to be refined. The objective of Fig. 6 was to justify the use of a coarser grid of 50 million cells (as it is as accurate as the fine 200 million-cell grid) for computing the laminar base flow in which the roughness element will be placed. The wall heat-flux patterns appear to agree well upstream of the roughness insert.

Performing scale-resolved DNS over the entire domain would lead to a prohibitively expensive grid. To capture transition induced by the roughness and keep the computational cost affordable, overlapping grids with two cells' overlap are generated and used with elsA. This chimera technique is called "patch assembly" [25]. The numbers of cells and grid sizes used for each element are gathered in Table 2. A coarse grid of 50 million cells is thus used around the forebody. A fine grid of 35 million cells is used around the diamond-shaped roughness element. A refined domain containing 255 million cells is added near the roughness and in its wake, so as to capture the roughness-induced instabilities leading to transition. The overlapping grids system can be seen in Fig. 4. This meshing strategy enables the DNS constraints to be met within the refined domains. The highest value of mesh sizes is found to be $\Delta x^+ = 7$, $\Delta y^+ = 5$, and $z^+ = 0.5$ in a turbulent region for the first cell above the wall.

D. Local Stability Analysis

LST-2D calculations are carried out following the classical linear stability theory [26] in order to determine the shape function, wave number, and growth rate of the unstable linear modes. The method

was first used for the analysis of roughness element wakes in a compressible boundary layer by Choudhari et al. [27] and was recently seen in the work of Montero and Pinna [28], who performed LST-2D in the wake of a cuboidal roughness element on a flat plate. The flow variables $q = [u, v, w, \rho, p]^T$ are decomposed into a steady reference state \bar{q} , also known as the base flow, and a small unsteady perturbation field q' . The assumption is made that the base flow is locally parallel in the streamwise direction and that the amplitude of the perturbations is a function of both x and z . The LST-2D used in this work was done with the code Bigsam [29]. The unsteady modal perturbations may be written as

$$q'(x, y, z, t) = \hat{q}(y, z) \exp[i(\alpha x - \omega t)] + c.c \quad (5)$$

where \hat{q} is a vector representing the two-dimensional amplitude functions. In the present spatial method, α is the complex wave number along the streamwise direction, ω is real and represents the angular frequency, and *c.c.* is the complex conjugate. The results in this paper are based purely on the spatial theory. The real part of α is the streamwise wave number $\alpha_r = 2\pi/L_x$, whereas its imaginary part represents the spatial damping/growth rate, where a positive value of α_i means a spatial decay of the amplitude function and a negative value means an exponential growth of q' along x .

The base-flow solution obtained with elsA is then interpolated on a Chebyshev–Gauss–Lobatto collocation grid by means of a cubic spline interpolation in each spatial direction. The generalized eigenvalue problem is solved by using the iterative Arnoldi method.

E. Spectral Proper Orthogonal Decomposition

The spectral proper orthogonal decomposition (SPOD) described in the early work of Lumley [30] was used for extracting the most energetic modes from the DNS flowfield. SPOD is estimated from a time series of two-dimensional snapshots using Welch's method. First, the data are segmented into a number of n_b overlapping blocks of 50% overlap, consisting of m_{FFT} snapshots each, and the temporal Fourier transform of each block l

$$\hat{X}^{(l)} = [\hat{x}(\omega_1)^{(l)} \quad \hat{x}(\omega_2)^{(l)} \quad \dots \quad \hat{x}(\omega_{m_{\text{FFT}}})^{(l)}] \quad (6)$$

is calculated. All blocks of the Fourier transform at a specific frequency ω_k are then collected into a new data matrix:

$$\hat{X}_{(\omega_k)} = [\hat{x}(\omega_k)^{(1)} \quad \hat{x}(\omega_k)^{(2)} \quad \dots \quad \hat{x}(\omega_k)^{(n_b)}] \quad (7)$$

The product $\hat{X}_{(\omega_k)} \hat{X}_{(\omega_k)}^T$ forms the cross-spectral density matrix, and its eigenvalue decomposition

$$\begin{aligned} \hat{X}_{(\omega_k)} \hat{X}_{(\omega_k)}^T \Phi_{\omega_{k,j}} &= \lambda_{\omega_{k,j}} \Phi_{\omega_{k,j}} \\ \lambda_{\omega_{k,1}} &\geq \dots \geq \lambda_{\omega_{k,n_b}} \geq 0 \end{aligned} \quad (8)$$

gives the SPOD modes $\Phi_{\omega_{k,j}}$ and the corresponding modal energies $\lambda_{\omega_{k,j}}$.

III. Simulation Validation

A. Wall Heat Flux

The thickness of the TSP coating was approximately 70 μm near the roughness insert. During tunnel operation, the TSP is illuminated with two blue LED arrays. A Cooke Corporation PCO.1600 14-bit

Table 2 Grid sizes for each element of the overlapping grids system

	Forebody	Isolated trip	Trip array	Refined domain
Number of cells ($\times 10^6$)	50	35	70	255
$[\Delta x_{\min}, \Delta x_{\max}]$ (mm)	[0.03, 1.0]	[0.001, 0.02]	[0.001, 0.035]	[0.07, 0.08]
$[\Delta y_{\min}, \Delta y_{\max}]$ (mm)	[0.03, 0.5]	[0.001, 0.02]	[0.001, 0.031]	[0.04, 0.05]
$[\Delta z_{\min}, \Delta z_{\max}]$ (mm)	[0.001, 1.0]	[0.001, 0.01]	[0.001, 0.018]	[0.001, 0.06]

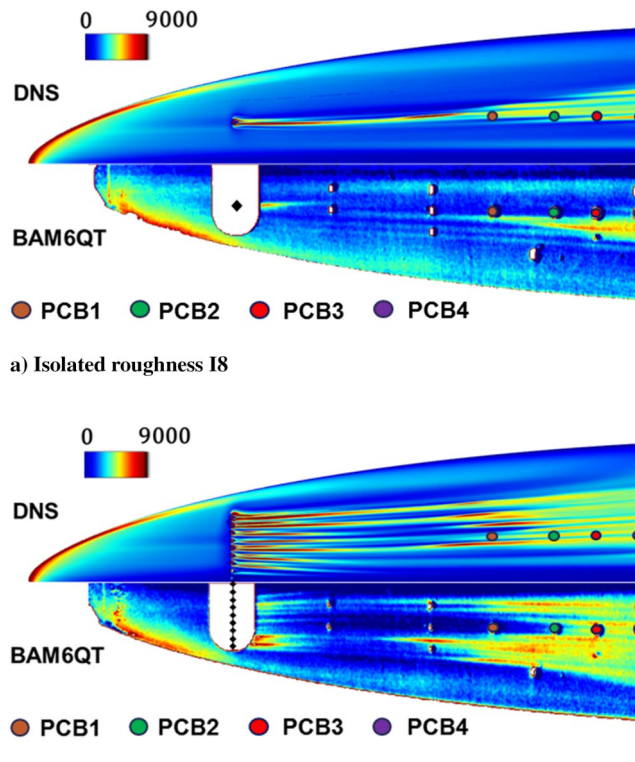


Fig. 7 Comparison of the time-averaged surface heat flux in W/m^2 , averaged over 4 ms.

CCD camera captures the images at 30 Hz, and the exposure time for each image is usually around 9 ms. Further details regarding the experimental apparatus can be found in Ref. [17]. The computational wall heat flux was averaged in time over 4 ms. The resulting comparison is shown in Fig. 7.

Favorable agreement is obtained for the isolated roughness I8 configuration. The values of the heat-flux contours are similar, and a similar shape of the turbulent wedge is obtained. However, transition seems to happen earlier in the DNS as the transition front is located closer to the roughness element. This difference could be explained by a potential misalignment of the forebody model in the tunnel. Asymmetry of the heat-flux patterns could be observed in the wind-tunnel runs involving a row of roughness elements [17]. This is due to the model being slightly yawed with respect to the freestream. The uncertainty on the angle of attack and yaw angle was estimated to be around 0.2 deg, based on model tolerance, alignment, and local deviations of the freestream. Previous studies in the BAM6QT [31] on cones estimated that the typical angle of attack uncertainties were between 0.2 and 0.5 deg, based on differences in the measured second-mode peak frequency. If the model were perfectly aligned with the freestream, it is likely that better agreement would be obtained in the transition front location. The longitudinal streaks in the laminar region can be observed in the TSP image and are found at the same spanwise location as with the simulations. On the other hand, the heat-flux level in this part is larger in the DNS, and the longitudinal streak patterns sustain over a larger distance. This is attributed to the higher spatial resolution of the simulations compared to the spatial resolution resulting from the postprocessing of the TSP. The experimental setup and postprocessing of the TSP images lead to a spatial resolution of 1 pixel for 0.41 mm. This is 10 times coarser than the computational grid.

In the R8 case, as the vortices generated by each roughness element interact with each other, the prediction of the wall heat flux appears to be more challenging. In this laminar region, the magnitude of heat flux is once again larger in the DNS results, which is consistent with the previous isolated roughness case. On the other hand, reasonable agreement is obtained in terms of which roughness elements induce the strongest heat-flux patterns. Two to three turbulent wedges can be

observed in the experimental and numerical results. Reasonable agreement is reached in the streamwise and spanwise location of their transition front. This can be easily seen, for instance, with the location of the turbulent wedge close to the symmetry plane of the forebody, with respect to the PCB sensor locations.

The wall heat-flux results obtained with the DNS are overall in favorable agreement with the experimental TSP images, which is quite satisfying given the complexity of the configuration. This validates the use of overlapping grids with the chimera method for predicting wall heat-flux patterns and whether or not transition will occur.

B. Wall-Pressure Fluctuations

The PCB sensors used in the experiments shown in Fig. 7 are PCB 132A31 piezoelectric pressure transducers. The PCB signals were sampled at 2.5 MHz. The sensors are 3.18 mm in diameter, with a sensing area of about 1.61 mm^2 . The large size of the PCB sensor with respect to the DNS grid size ($\Delta_y^+ = 80$) motivates the extraction of the DNS signal at different spanwise locations over the PCB lateral extent. Hence, five local signals were extracted at several spanwise locations: $y = [y_{(\text{PCB})}, y_{(\text{PCB})} \pm 0.75 \text{ mm}, y_{(\text{PCB})} \pm 1.5 \text{ mm}]$ and averaged. This is useful in accounting for the spanwise variation of the wall-pressure fluctuations. The power spectral density (PSD) spectra were computed using Welch's method with 20 overlapping segments of 512 points with 50% overlap.

As shown in Fig. 8, the frequency peak at $f = 180 \text{ kHz}$ obtained for PCB1 and PCB3 is accurately captured in the wake of the isolated roughness element I8, although the PSD value is higher in the experiments. The peak observed at $f = 45 \text{ kHz}$ at PCB1 is also well-captured. The PSD level is well-predicted at all PCB sensors, and the slope of the PSD curves in the high frequencies $f > 250 \text{ kHz}$ is the same in the experiments as in the DNS. The main discrepancies are found in the low frequency region $f < 30 \text{ kHz}$ as well as in the prediction of the peak-amplitude frequency obtained in PCB4, where the DNS predicts a lower frequency.

Reasonable agreement is also obtained for the R8 configuration for PCB1, PCB2, and PCB3, as shown in Fig. 9. The spectral distribution is similar. At the PCB1 sensor location, the peak obtained at $f = 180 \text{ kHz}$ is relatively well-captured by the DNS. The rapid decay for high frequencies in the experiment is also observed in the computations. The high-frequency decay in PSD values has the same slope at PCB1, PCB2, and PCB3 locations. At PCB4 however, the curves exhibit differences from $f = 300 \text{ kHz}$. Differences are still observed at high frequency, for $f > [300-400] \text{ kHz}$ at all PCB locations. This is explained by the fact that PCB sensors are not meant to provide a flat dynamic response beyond 300 kHz but considerably less. The flatness of the experimental data at PCB1 and PCB2 at high frequency appears like an electronic noise floor.

This favorable comparison with the experiments gives confidence in the numerical strategy used as well as the following analysis of roughness-induced transition mechanisms.

IV. Stability on the Smooth Forebody

The study of roughness effect on the scramjetlike forebody is quite complex, as the flow around the smooth forebody carries its own underlying physical mechanisms. Prior to studying the linear instabilities of the roughness wake, it is necessary to shed light on the structure of the flow over this smooth forebody. LST-2D computations were thus performed at three streamwise locations $x = [120, 160, 220] \text{ mm}$. The domain used in the LST-2D computations extends over the flat portion of the forebody, that is, between the symmetry plane and the swept leading edge, so as to include the streamwise vortex in the midspan. The Mack mode is the most unstable mode at each computed streamwise location. The growth rate is shown as a function of frequency in Fig. 10. The peak frequency f decreases with increasing streamwise distance, following the relation: $St = f\delta/U_e \approx 0.4$, where δ is the boundary-layer thickness and U_e is the edge velocity.

The shape of this Mack mode is shown in Fig. 11. At each streamwise location, the pressure and streamwise velocity eigenfunctions are both represented at the peak frequencies. The eigenfunctions were

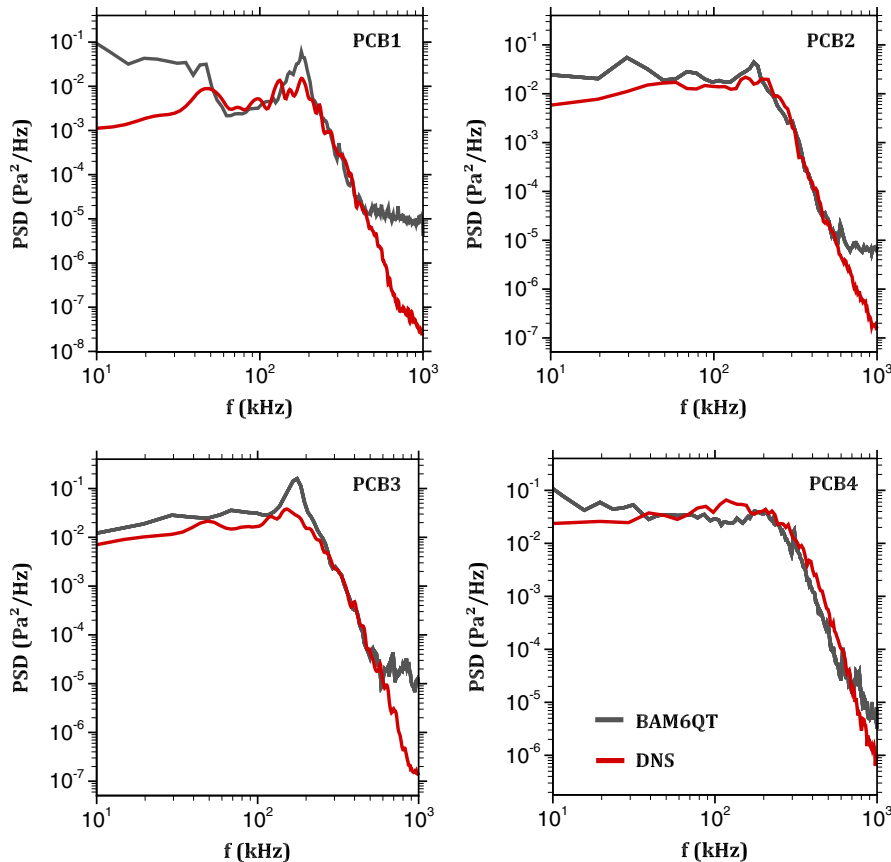


Fig. 8 Comparison of the power spectral density at the experimental PCB sensors' location for an isolated roughness element I8.

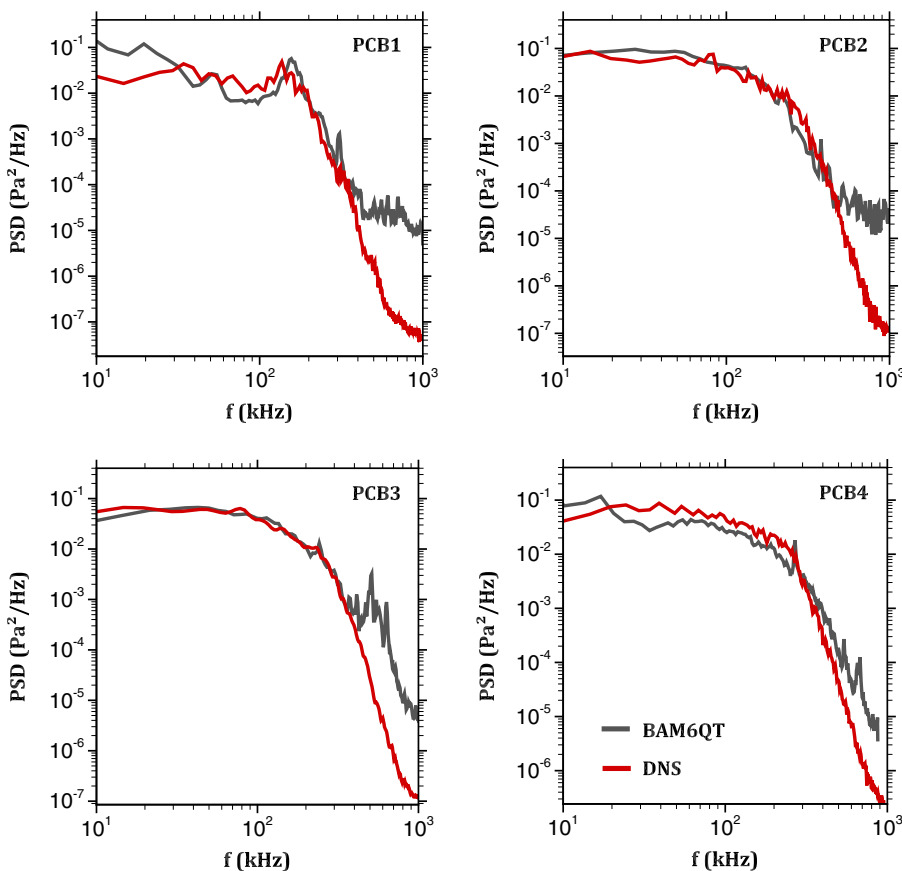


Fig. 9 Comparison of the power spectral density at the experimental PCB sensors' location for a row of roughness R8.

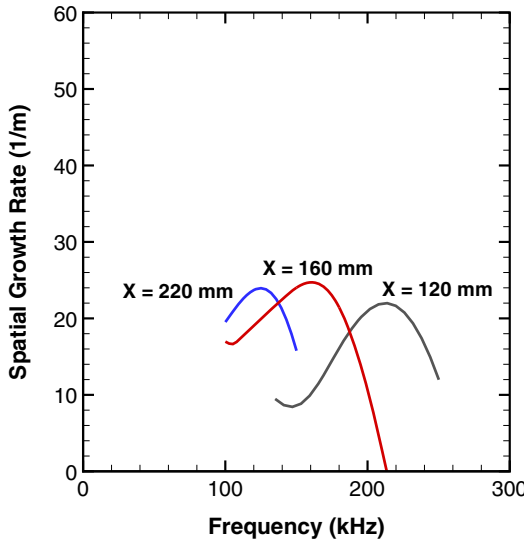


Fig. 10 Growth rates as a function of frequency for most unstable modes at several streamwise stations.

normalized by their maximum value at each streamwise station. The basic state streamwise velocity contours are indicated via black lines. The mean heat flux is also shown on the smooth forebody surface. The peak magnitude of the mode is located in the streamwise vortex at nearly the same spanwise location as where the roughness will be. Hence, it is likely that it will be modified by the roughness-induced flow features.

V. Results for the Isolated Roughness I8

A. Roughness-Induced Laminar Base Flow

The base-flow topology is depicted in Fig. 12a. The roughness induces two separated flow regions, immediately upstream and downstream of the roughness element, shown in Fig. 12a with red isosurfaces of infinitesimally small negative velocity. The shape of the recirculation regions resembles the one induced by a roughness immersed in a Blasius boundary layer, except it is slightly yawed.

The near-wall streamlines along the forebody show motion of the fluid from the attachment line towards the symmetry plane. As a result,

the base flow in which the isolated roughness is immersed holds a spanwise component of the velocity. As observed in the close-up of Fig. 12a, the interaction between the roughness element and the span-inhomogeneous base flow leads to the formation of a counter-rotating vortex pair at $x = 0.105$ m. These vortices quickly merge and evolve towards a crossflowlike vortex at $x = 0.120$ m. The rotation of the fluid around the vortex core is characterized by the helical motion of the streamlines in the roughness wake. These streamlines were chosen from points within the center of the crossflowlike vortex at $x = 0.120$ m. The counter-rotating vortex pair, inducing longitudinal streaks that are typically found in the wake of isolated roughness elements in a span-homogeneous flow, does not hold for a long distance. Thus it is likely that the transition mechanisms will be different from the classical symmetric and antisymmetric instabilities.

As shown in Figs. 12b and 12c, high values of spanwise and wall-normal velocity gradients are found around this crossflowlike vortex. The spanwise gradients are mainly concentrated on the shoulder of the crossflow vortex, whereas the wall-normal gradients are located on its trough. The presence of this high-shear layer is associated with highly unstable modes as will be discussed in the next part.

B. Linear Instabilities of the Roughness Wake

As the vortex pattern in the wake of the isolated roughness element is compact, that is, located in a narrow region, it is possible to apply LST-2D calculations without getting spurious modes originating at the boundaries. In this work, we focus only on the disturbances of the main vortex, as it is found to be where the peak fluctuations are located and where transition occurs first. Unstable modes present in the surrounding boundary layer are thus not studied here. Note that controlled freestream disturbances are not applied in the current work. The unsteadiness is found to be due to the interaction between the roughness-induced shear layer and the crossflowlike vortex, and there could be a feedback loop instability as in Shrestha and Candler [10]. The main focus here is on the high-frequency disturbances, which are linked more closely with the observed onset of laminar breakdown in the unsteady calculations. This can be observed in Fig. 13 where the turbulent kinetic energy integrated over the spanwise extent of the refined domain at different streamwise positions is shown as a function of frequency. The amplitude of the disturbances is the highest at $f = 135$ kHz, $f = 180$ kHz, and $f = 265$ kHz. The turbulent kinetic energy appears to be the highest at $f = 265$ kHz for all streamwise locations.

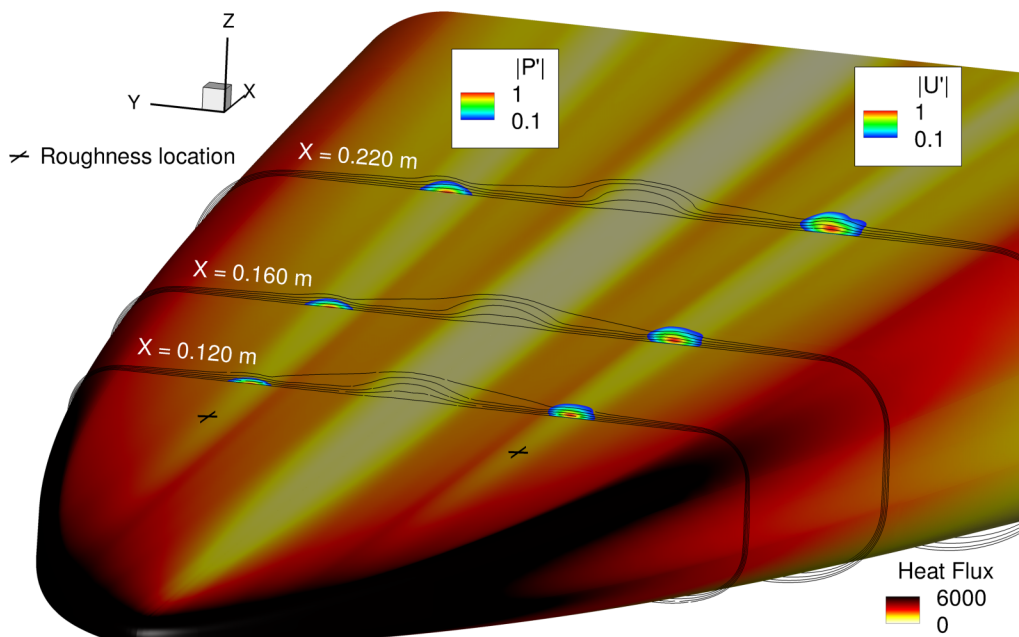
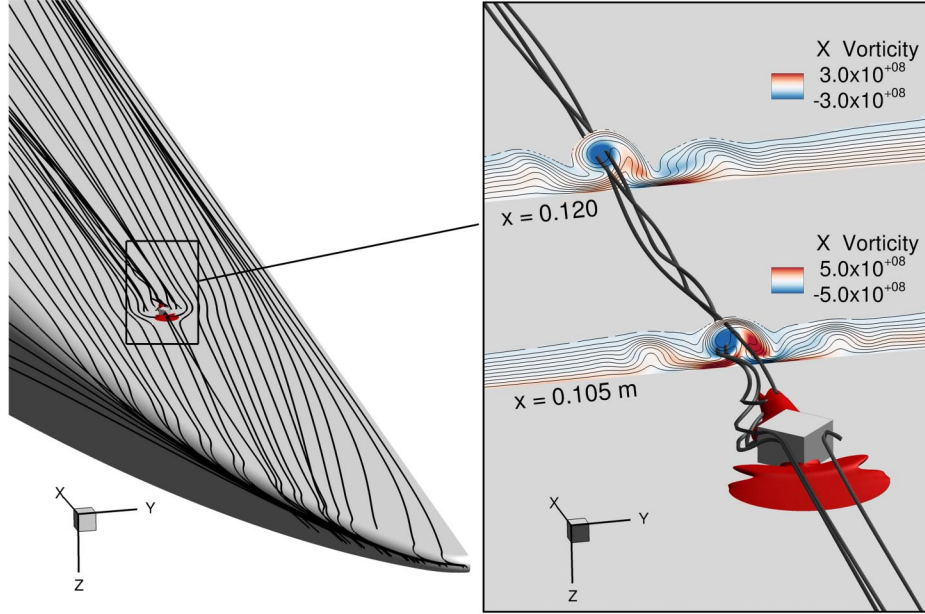
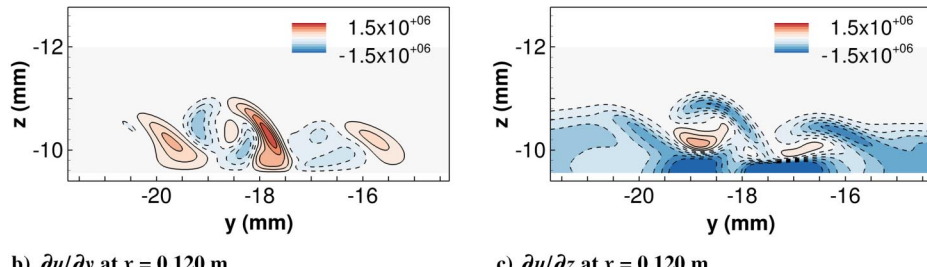


Fig. 11 Contours of Mack mode $|u'|$ and $|p'|$ eigenfunctions at peak growth rate frequencies for the smooth forebody configuration. Basic state streamwise velocity contours are indicated via black lines. The mean heat flux is also shown on the smooth forebody surface.



a) Near-wall velocity streamlines (left) and three-dimensional streamlines (right). The red isosurfaces are upstream and downstream recirculation regions



b) $\partial u / \partial y$ at $x = 0.120$ m
c) $\partial u / \partial z$ at $x = 0.120$ m

Fig. 12 Roughness-induced base flow.

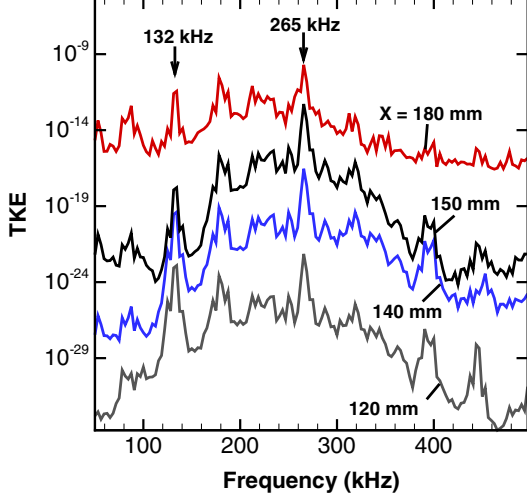


Fig. 13 Turbulent kinetic energy integrated over the spanwise extent of the refined domain at different streamwise positions as a function of frequency.

Due to the spanwise component of the basic state velocity, the trajectory of the main vortex is not aligned with the direction of the freestream. Therefore, LST-2D computations are conducted in two-dimensional planes perpendicular to the main vortex trajectory. To get insight into the dominant unstable modes present in the wake of the roughness element, the stability analyses are first conducted at a

single streamwise location $x = 0.120$ m. The spatial growth rates are shown in Fig. 14a. A total of three dominant high-frequency modes were selected, namely a Mack second mode, a helical mode, and a secondary instability of the finite-amplitude crossflow vortex induced by the roughness. In all stability computations shown in this work, the main crossflow vortex was discretized with a 45×45 grid. The accuracy of these calculations was verified on finer grids in both spanwise and wall-normal directions. Triangle-shaped symbols shown in Fig. 14a represent the results obtained with a 60×60 grid around the main vortex. The peak growth rate of both the helical and Mack modes is reached around 235 kHz, whereas the secondary instability is the most unstable around 275 kHz. The range of unstable frequencies associated is very broad, extending from almost 0 kHz to over 600 kHz. As explained in Ref. [15], the large frequency bandwidth of this mode appears consistent as it lies in the relatively thin, inclined shear layer associated with the overturning contours of axial velocity from the strong crossflow vortex. Its shape and location are similar to the "z" mode obtained in previous stability studies in swept-wing three-dimensional boundary layers [32]. The phase speed of each mode is shown in Fig. 14b. The phase speed of the helical mode is much lower than the other two modes, whereas the phase speeds of the Mack mode and secondary instability remain higher than $0.8U_e$. The mode shapes of each dominant mode will now be discussed in the following sections, moving from the least unstable to the most unstable mode.

C. Mack Mode

The contours of second-mode (i.e., Mack mode) $|u'|$ and $|p'|$ eigenfunctions at peak growth rate frequency $f = 235$ kHz and $x = 0.120$ m are shown in Fig. 15. The red line corresponds to the sonic

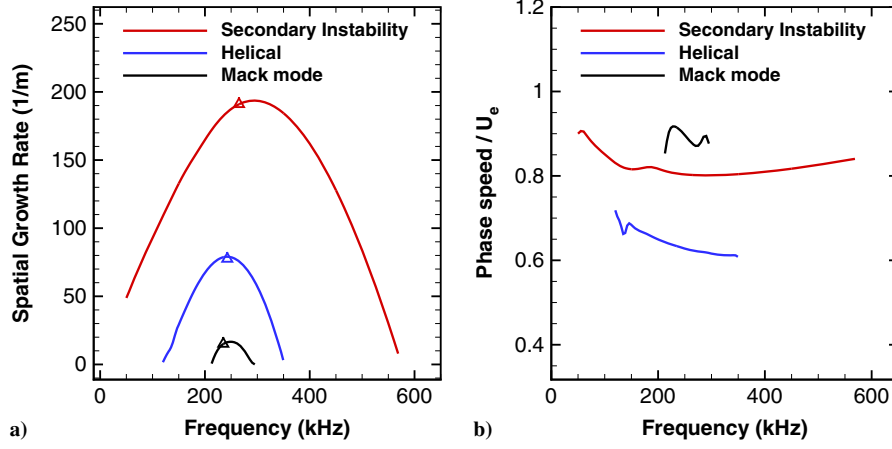


Fig. 14 a) Growth rates and b) phase speed scaled by edge velocity as function of frequency for dominant instability modes at $x = 0.120 \text{ m}$. The triangle-shaped symbols were obtained with a fine 60×60 grid for the discretization of the main vortex.

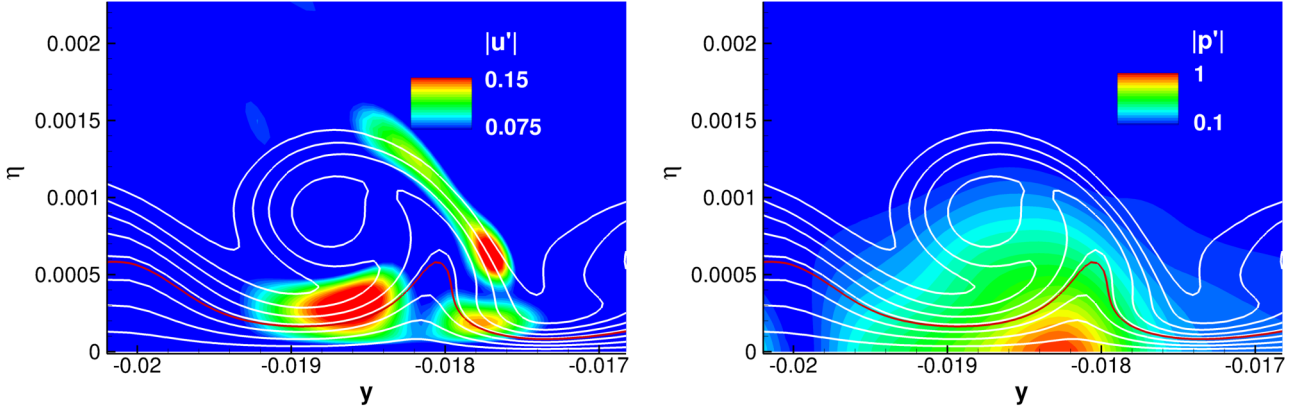


Fig. 15 Contours of Mack mode $|u'|$ and $|p'|$ eigenfunctions at peak growth rate frequency $f = 235 \text{ kHz}$ and $x = 0.120 \text{ m}$. Basic state streamwise velocity contours are indicated via white lines. The red line shows the sonic line. The wall-normal distance is η .

line. The peak pressure fluctuations are concentrated between the wall and the sonic line, and the streamwise velocity eigenfunctions lie in the lower part of the crossflow vortex, just above the sonic line. This is consistent with its definition as an acoustic wave trapped in the relative supersonic region [33]. It is worth noticing that the $|p'|$ eigenfunctions have a peak near the surface only in the Mack mode case. Likewise, the PSD in Fig. 8 shows only a peak near 180 kHz, so it looks as if the experiments capture the Mack mode effects more than the secondary instability. It was observed in the LST-2D results over the smooth forebody in Section IV that this mode was present even in the absence of roughness on the smooth forebody boundary layer. As explained by De Tullio and Sandham [34], the roughness element mainly acts as a disturbance amplifier as the roughness-induced stationary crossflow vortex strongly modulates the shape of this Mack mode.

In the works of [11,15,16], the Mack modes appeared to be the only high-frequency traveling disturbances unstable at the initial stages of the growth of the crossflow vortices. As the crossflow vortices grew in the roughness wake, the Mack mode was found to be modulated by the crossflow vortex and to morph into the shear layer instability, such that it was not possible to differentiate between the Mack modes and the shear layer instabilities at the downstream locations. A similar behavior could be observed for Goertler vortices [35,36], for the centerline vortex on the elliptic cone [37], or the crossflowlike vortex over the Boundary-Layer Transition flight experiment (BOLT) geometry [38].

D. Helical Instability

Figure 16 shows the mode shapes of the helical mode. The eigenfunctions u' , v' , and w' were normalized such that the magnitude of

the peak p' fluctuation across the vortex is equal to unity. The fluctuations of this mode are concentrated inside the crossflow vortex, in its downwelling part. It is composed of a single spiral which makes it an $m = 1$ mode. The spiral in Fig. 16 is drawn from $[v', w']$ streamlines. The helical instability was found with LST-2D at different axial stations to measure the global contribution of this mode in the transition process. Figure 17 plots the spatial growth rate of the helical mode between $x = 0.105 \text{ m}$ and $x = 0.120 \text{ m}$. The instability rapidly grows before reaching its maximum growth rate at $x = 0.110 \text{ m}$. It then decreases in growth rate and becomes stable from $x = 0.125 \text{ m}$.

Even though the spatial growth rate of the mode is high, no helical mode was found with the SPOD analysis of the unsteady simulation. This is attributed to the fact that it is unstable only in a very small region $x \in [0.105; 0.120]$ compared to the linear part of the flow $x \in [0.110; 0.170]$ and because of the dominance of the secondary instability of the crossflow vortex. However, the helical instability may play a key role in the unsteadiness of the near region of the roughness wake.

The peak frequency of this mode increases with increasing streamwise distance, which limits the maximum amplitudes that can be reached, contrary to the secondary instability of the following crossflow vortex, which remains in the same frequency band.

E. Secondary Instability

The mode shapes of the secondary instability of the finite amplitude crossflow vortex are shown in Fig. 18 at $f = 265 \text{ kHz}$ with $x = 0.120 \text{ m}$. They are compared with the dominant mode obtained from SPOD of the unsteady simulation. The SPOD results shown here were obtained using a total number of $N_{\text{FFT}} = 2560$ snapshots,

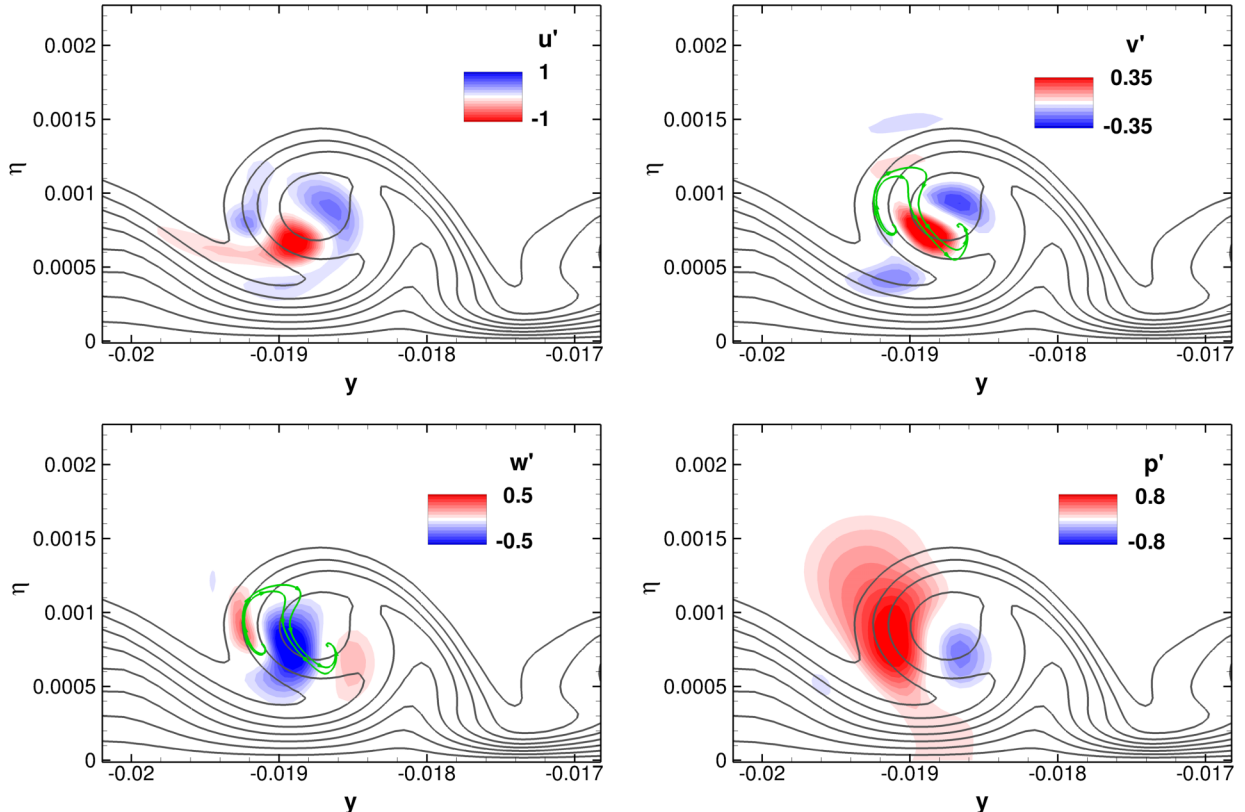


Fig. 16 Contours of helical mode eigenfunctions at peak growth rate frequency $f = 235$ kHz at $x = 0.120$ m. Streamlines are included based on v' and w' , showing the location of the helical mode, and η is the wall-normal distance.

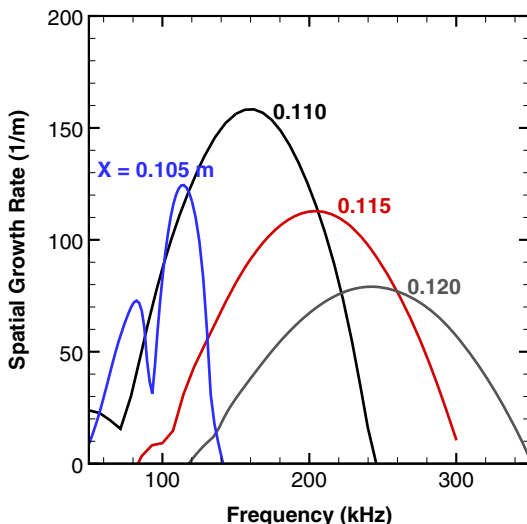


Fig. 17 Streamwise evolution of helical mode growth rate between $x = 0.105$ m and $x = 0.120$ m.

sampled at a frequency of $f_s = 1.5$ MHz. The data were segmented into a number of nine overlapping blocks of 50% overlap, consisting of $m_{FFT} = 512$ snapshots each. Segmenting the data into 15 overlapping blocks with $m_{FFT} = 256$ each did not show any difference in the results; the secondary instability mode contains 99.9% of the total modal energy and no helical mode could be obtained. Streamwise velocity $|u'|$ and pressure $|p'|$ eigenfunctions were normalized to unity for comparison. The peak fluctuations are found in the thin, curved shear layer. The agreement between SPOD and LST-2D is very good. The peak fluctuations are predicted at the same location and spread following the same shape. This validates the linear stability approach for finding the mode shapes, given that the most unstable mode corresponds to the dominant SPOD mode.

Mode shapes of $|p'|$ perturbations at selected locations from the dominant SPOD mode and the LST-2D predictions for the secondary instability at the same locations are shown in Fig. 19, respectively. Good agreement between SPOD and LST-2D is once again observed in terms of mode shapes in the linear part of the flow. At $x = 0.180$ m, the exponential growth of disturbances starts reaching saturation, indicating the occurrence of nonlinear interactions. The agreement between the SPOD and LST-2D mode shapes remains good at this streamwise location, even though base-flow modifications start to be observed.

The streamwise evolution of the leading secondary instability mode growth rate predicted by LST-2D is shown in Fig. 20a. The local growth rate decreases between $x = 0.110$ m and $x = 0.180$ m, but the mode stays unstable. The range of unstable frequencies is broad for all axial stations, extending from almost 0 kHz to over 600 kHz. For a given frequency, the difference between the N-factor at x and the N-factor at $x_0 = 0.12$ m is computed to be able to compare the LST-2D results with the DNS results. It is defined as

$$N(x) - N(x_0) = \int_{x_0}^x (-\alpha_i(x')) dx' \quad (9)$$

Figure 20b shows a comparison of the N-factor streamwise evolution predicted by LST-2D and DNS. One can see that the N-factor obtained by both methods increases monotonically. We observe that the peak of the N-factor spectra is predicted at nearly the same frequency by DNS and LST-2D. The peak frequency predicted by DNS calculations is reached at $f = 265$ kHz whereas the LST-2D results predict a slightly higher peak frequency of $f = 275$ kHz. However, the N-factor based on LST-2D computations is lower than the DNS predictions. The N-factor at $x = 0.180$ m when transition occurs is equal to 8 in the DNS and 7.2 in the LST-2D. This was also observed in the work of Choudhari et al. [16] and De Tullio et al. [39], where the N-factor obtained with LST computations was below the one predicted by DNS and PSE. This is attributed to the high degree

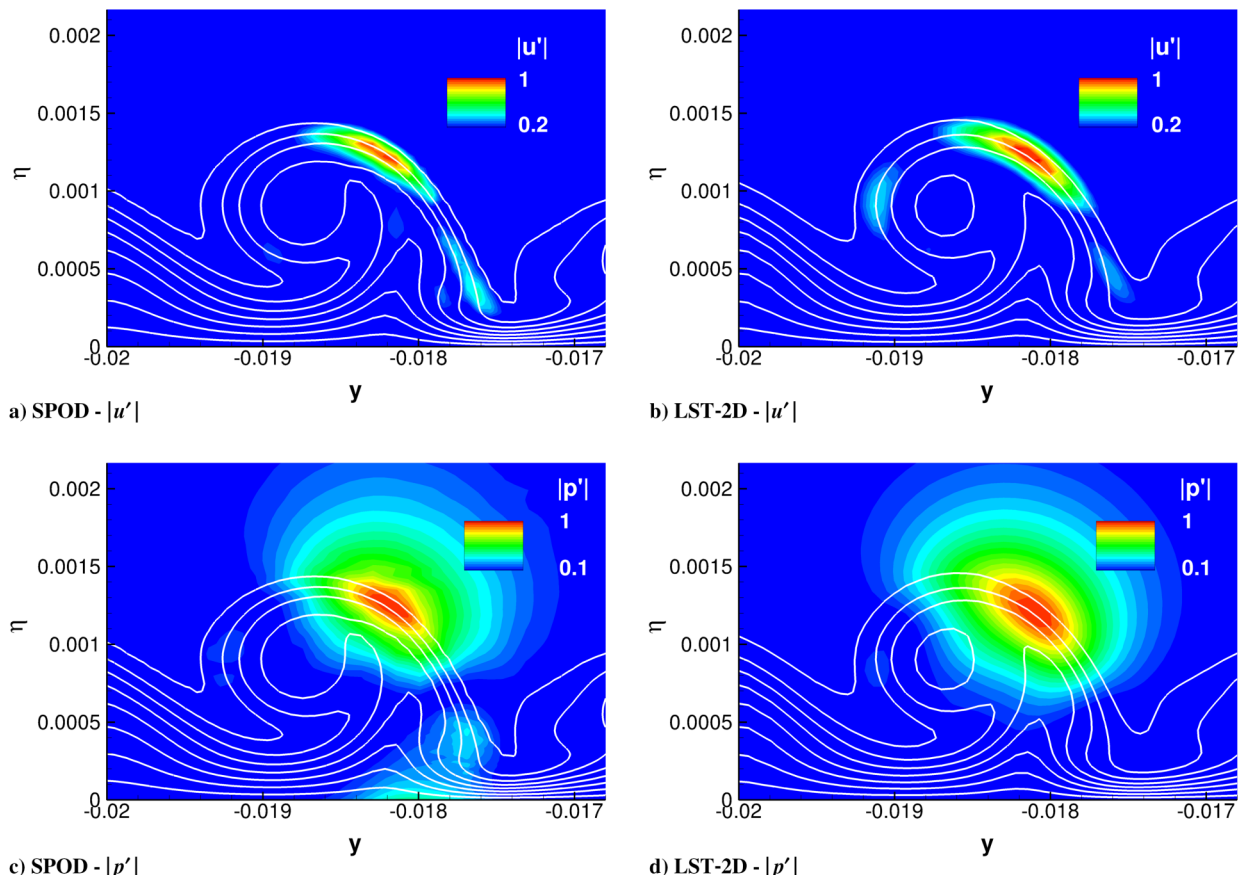
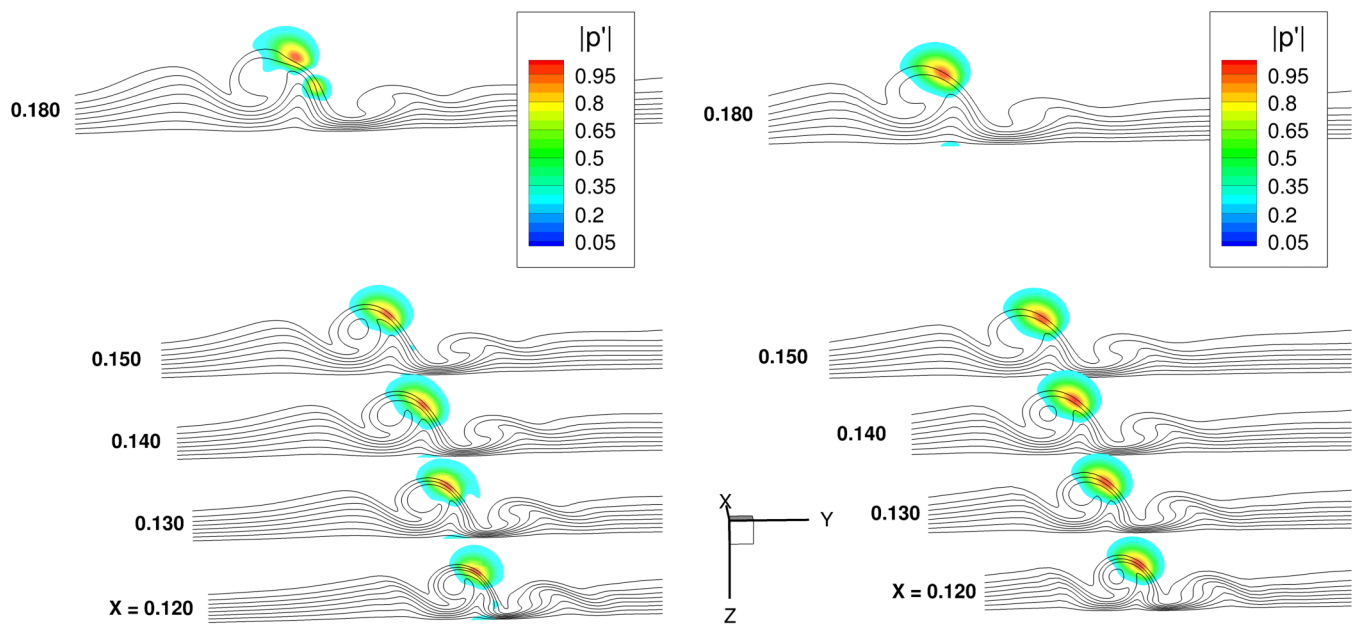


Fig. 18 Contours of $|u'|$ and $|p'|$ eigenfunctions normalized to unity for the secondary instability of the finite amplitude crossflow vortex. Comparison of the mode shapes obtained with SPOD and LST-2D at $f = 265$ kHz and $x = 0.120$ m. Basic state velocity contours are indicated via white lines.



a) SPOD

b) LST2-D

Fig. 19 Streamwise evolution of secondary instability mode shapes based on pressure fluctuations at $f = 265$ kHz. The peak fluctuation amplitude is normalized to unity at each axial station. The basic state streamwise velocity is shown via the black isolines.

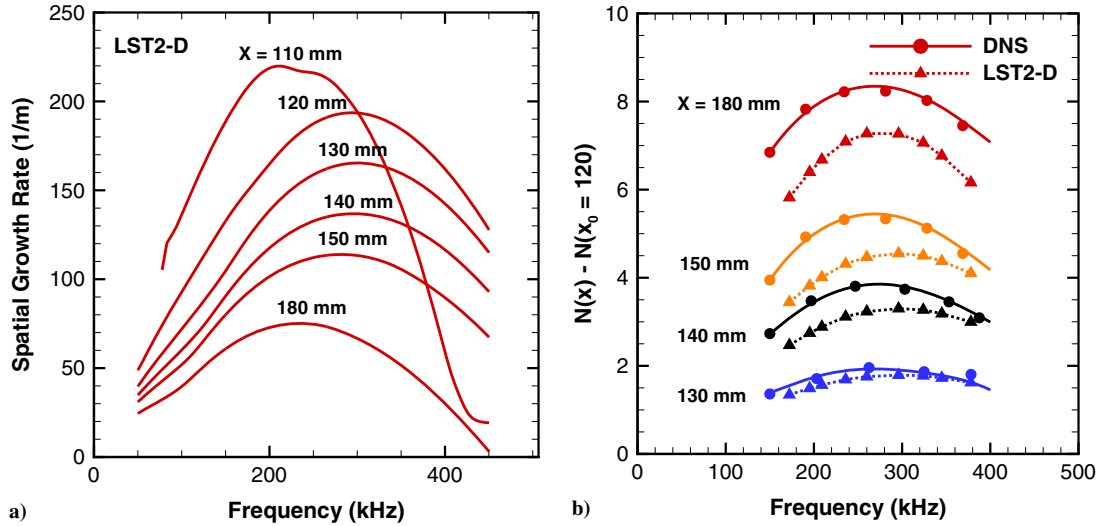


Fig. 20 Comparison of growth rate predictions: a) streamwise evolution of secondary instability mode growth rate predicted by LST2-D and b) N-factor evolution of the secondary instability mode computed with LST2-D and DNS.

of nonparallelism taking place in the wake of a roughness immersed in a flow holding a spanwise component of the velocity.

VI. Results for a Trip Array

A. Roughness-Induced Laminar Base Flow

The topology of the base flow induced by the trip array can be seen in Fig. 21. The streamwise vorticity and velocity gradients of the base flow are shown in the wake of the trip array at $x = 0.120$ m. For comparison, the streamwise vorticity and velocity gradients are also shown for the smooth forebody and the isolated roughness configurations. It can be seen that the row of roughness generates a large number of vortices, that is, a primary vortex and a second smaller vortex per roughness element. They are crossflowlike vortices that look like the main crossflow vortex found in the wake of the isolated roughness element. The values of streamwise vorticity and velocity gradients $\partial u / \partial y$ and $\partial u / \partial z$ also lie in the same range, but the trip array induces stronger gradients in the bottom part of the crossflow vortex shoulder. The high similarity in the

base flow features indicates that the most unstable modes will share similar characteristics with the isolated roughness case. Note that in the absence of roughness, the velocity gradients are weak, as $\partial u / \partial y$ is more than one order of magnitude smaller than in the roughness cases.

For each configuration, the upstream and downstream separated flow regions induced by the roughness are shown in Fig. 22. Let us recall that in the R8 configuration, the trip spacing ($s = 3.2$ mm) to roughness width ($D = 1.6$ mm) ratio is equal to $s/D = 2$. One can notice that due to the high proximity of the roughness elements to each other, the separated region upstream of each element influences its neighbors, resulting in a larger separated region than with the isolated roughness, which extends across the spanwise extent of the trip array. This is in good agreement with Ref. [40], where the extent of separation was found to decrease with increasing s/D .

B. Linear Instability of the Roughness Wake

Due to the large number of vortices present in the wake of the trip array, their interaction and the induced nonparallel flow make it

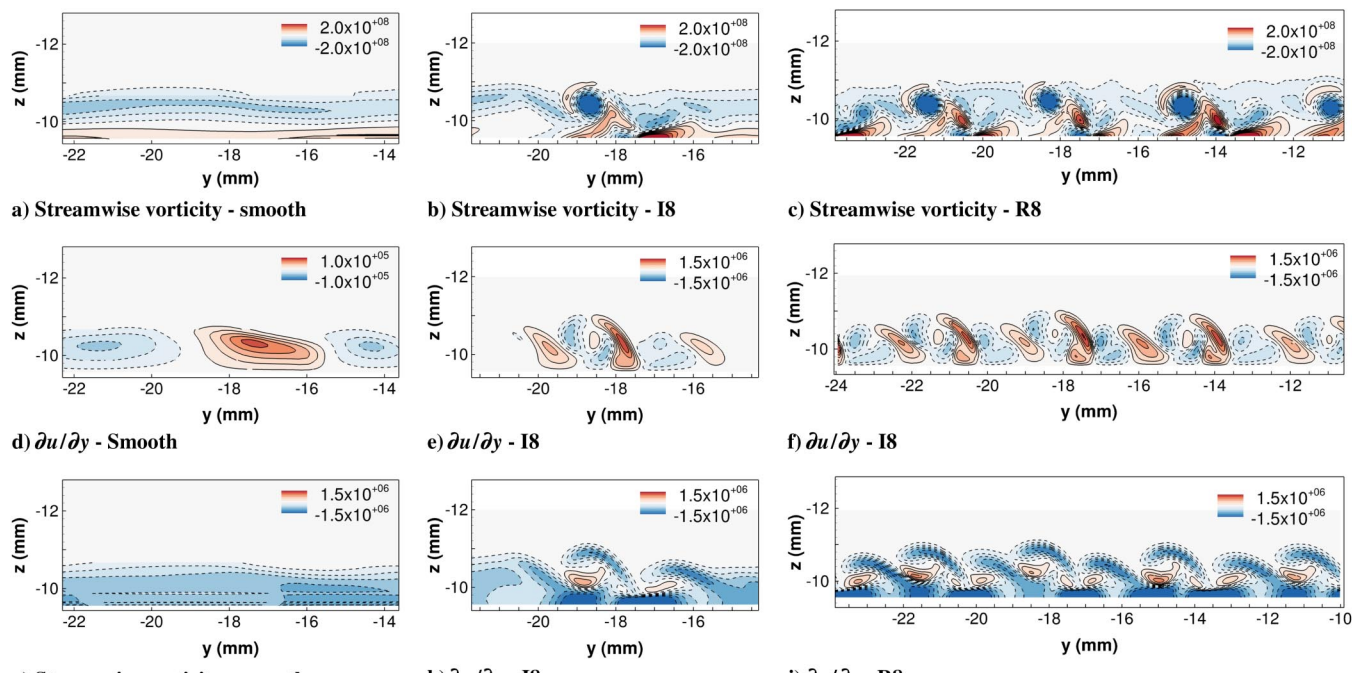


Fig. 21 Topology of the base flow induced by the smooth forebody (a, d, and g), the isolated roughness (b, e, and h), and the trip array (c, f, and i) at $x = 0.120$ m.

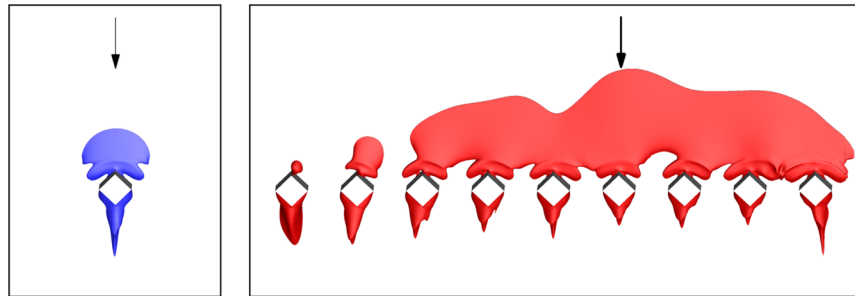


Fig. 22 Visualization of separated flow regions with isosurfaces of $u = -10^{-5} \text{ m} \cdot \text{s}^{-1}$.

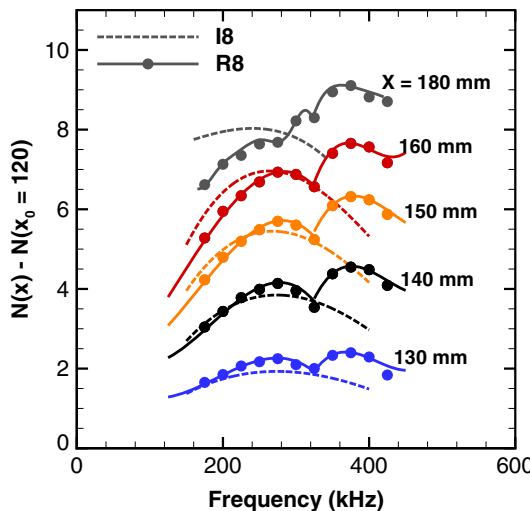


Fig. 23 N-factor evolution of the secondary instability mode induced by the trip array computed from DNS. The dashed lines correspond to the isolated roughness case.

difficult for the LST-2D method to be applied. Using the unsteady data obtained with DNS, the same methodology as for the isolated roughness case was used for determining the frequencies of the most unstable modes. The resulting N-factor spectra are shown in Fig. 23. The dashed lines correspond to the isolated roughness case. The N-factors achieved by the most unstable modes is slightly higher with the trip array and peak at a comparable frequency near 275 kHz. One can also observe the emergence of a higher-frequency mode being most unstable near 375 kHz. Note that the calculation of the N-factor spectra was integrated across the span so as to highlight the peak

frequencies of the dominant secondary instability modes. As the boundary-layer thickness is changing across the span, so does the frequency of the secondary instability.

The previous most unstable modes correspond to secondary instabilities of the stationary crossflow vortices. This can be seen in Figs. 24 and 25 where the mode shapes based on pressure fluctuations are shown at several axial stations at $f = 275 \text{ kHz}$ and $f = 375 \text{ kHz}$, respectively. The peak fluctuations are found at the same location as for the isolated roughness case, in the thin inclined shear layer. The mode at $f = 275 \text{ kHz}$ is located in the midspan of the forebody, in the shear layer of a crossflow vortex that sustains over a large streamwise distance, whereas the mode at $f = 375 \text{ kHz}$ is located in the outer crossflow vortices. At $x = 0.200 \text{ m}$, the shape of the secondary instability changes. One can also observe that as the flow moves downstream, the number of vortices decreases while their size increases. This is due to the coalescence of the vortices.

C. Comparison to the Isolated Roughness

Finally, the flow structures and tripping efficiency for the isolated roughness 18 and the row of roughness R8 are compared. Fig. 26 shows instantaneous isosurfaces of the Q criterion. In the transitional region, oblique hairpinlike structures are observed in both configurations. They are caused by the base-flow deformation due to the nonlinear development of the dominant secondary instability mode. They are slightly different from the hairpin vortices typically observed in parallel flows in the sense that their cross section is not perpendicular to the vortex trajectory. These structures rapidly break down, leading to a turbulent wedge that grows in the spanwise direction. The spanwise spreading of the turbulent wedge is larger with the isolated roughness. This is due to the interaction of the turbulent wake structures of the R8 configuration. The use of a trip array may be interesting as it leads to a wide turbulent region at the end of the forebody due to the merging of the different turbulent

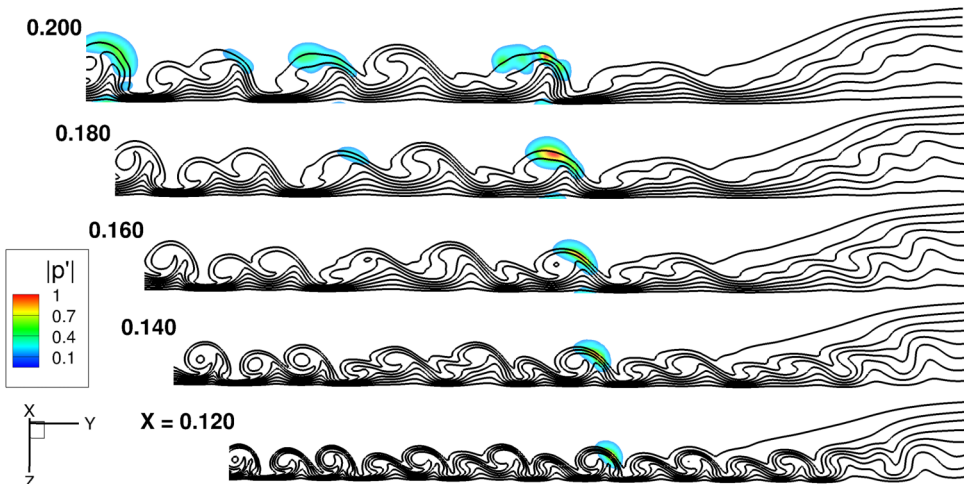


Fig. 24 Streamwise evolution of secondary instability mode shapes based on pressure fluctuations at $f = 275 \text{ kHz}$. The peak fluctuation amplitude is normalized to unity at each axial station. The basic state streamwise velocity is shown via the black isolines.

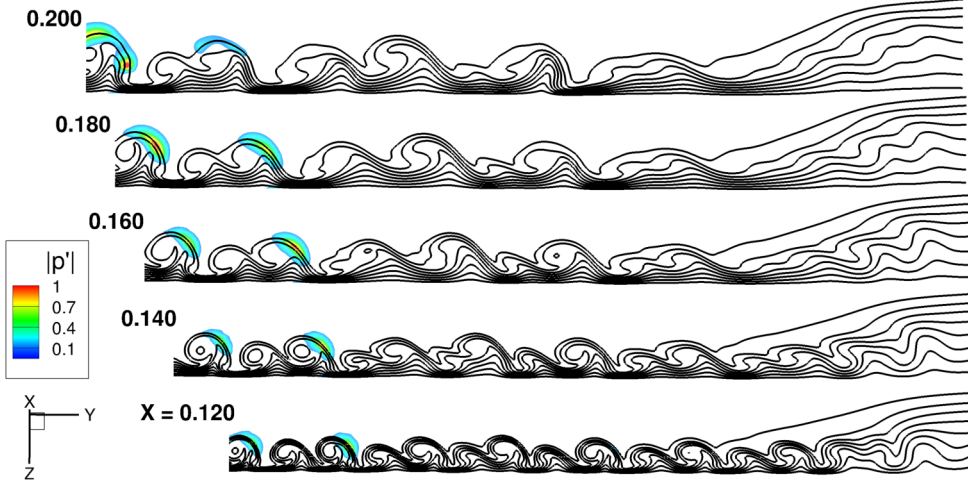
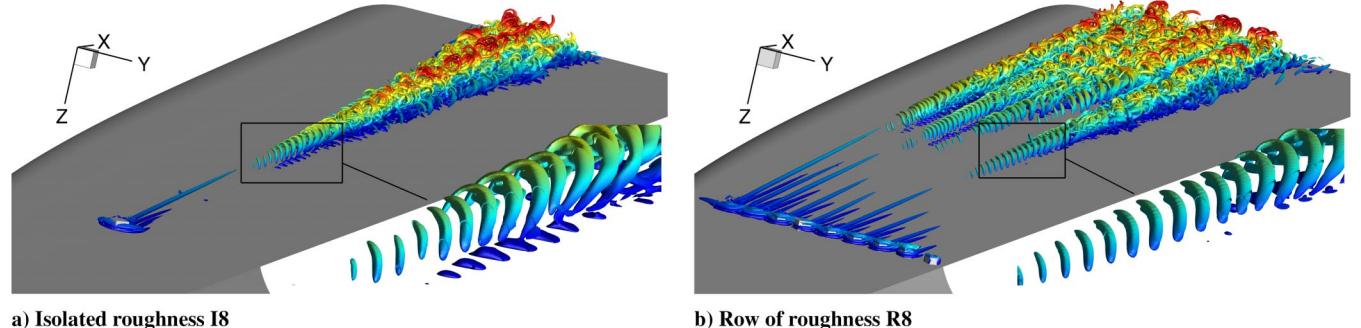


Fig. 25 Streamwise evolution of secondary instability mode shapes based on pressure fluctuations at $f = 375$ kHz. The peak fluctuation amplitude is normalized to unity at each axial station. The basic state streamwise velocity is shown via the black isolines.



a) Isolated roughness I8

b) Row of roughness R8

Fig. 26 Visualization of the roughness-induced turbulent wedge(s) after breakdown to turbulence. Isosurfaces of Q criterion $Q = 1 \times 10^5$ colored by distance from the wall.

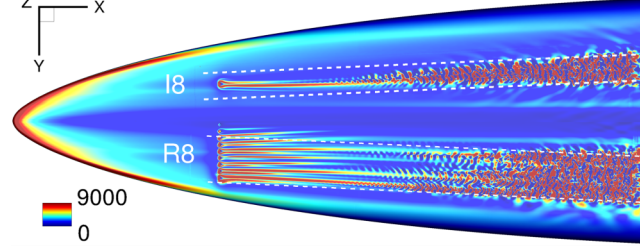


Fig. 27 Instantaneous surface heat flux in W/m^2 .

wedges. This can also be observed in Fig. 27 with the contours of instantaneous surface heat flux.

To examine the tripping efficiency of both configurations, the time-averaged skin-friction coefficient is compared. The skin-friction coefficient in Fig. 28 was averaged over the spanwise extent of the turbulent wake between the two white dashed-lines present in Fig. 27. It is defined as

$$C_f = \tau_w / \left(\frac{1}{2} \rho_\infty u_\infty^2 \right) \quad (10)$$

Upstream of the region of influence of the roughness element $x < 0.085$ m, the skin-friction value of the laminar boundary layer agrees well with Eckert's compressible laminar flow correlation [41], in which the correlation origin is taken at $x = 0.02$ m, which corresponds to the beginning of the flat portion of the forebody, aft the leading edge. The skin-friction coefficient upstream of the roughness

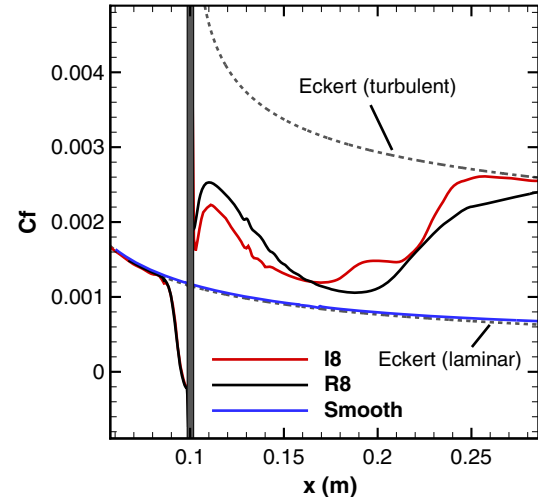


Fig. 28 Skin-friction coefficient comparison for the smooth forebody (Smooth), the isolated roughness (I8) and the trip array (R8) averaged in time and in span between the two white dashed-lines present in Fig. 27.

is the same in all cases, which means that the spanwise extent of the averaging is appropriately chosen. Downstream of the roughness element, the skin friction rises sharply from $x = 0.200$ m for the trip array and at $x = 0.180$ m for the isolated roughness, indicating the onset of transition. We observe that the flow becomes transitional earlier in the isolated roughness configuration. After breakdown to turbulence, the skin-friction values are found to agree well with

Eckert's turbulent correlation when the correlation origin is set to the roughness location $x = 0.100$ m. Eckert's turbulent correlation [41] is computed as

$$C_f = \frac{0.0592}{Re_{x^*}^{0.2}} \quad (11)$$

Given that the extent of the turbulent wake is very different in each case, it is difficult to determine which configuration is the most efficient in tripping the boundary layer. When looking at the streamwise evolution of the skin-friction coefficient, it seems like transition occurs earlier in the isolated roughness case. However, this highly depends on the spanwise extent chosen for averaging the skin-friction coefficient. Hence, no definite conclusion can be drawn regarding the tripping efficiency performed by both configurations, using the span-averaged skin-friction coefficient. On the other hand, the comparison of time-averaged heat flux shown in Fig. 7 suggests that the roughness array configuration is more effective in tripping the boundary layer, as the transition front appears closer to the trips.

VII. Conclusions

Direct numerical simulations have been performed on a realistic configuration of hypersonic vehicle forebody to investigate the laminar-turbulent transition induced by a diamond-shaped roughness element. The purpose of this investigation was to identify and characterize the instabilities induced by an isolated roughness and by a trip array in the three-dimensional boundary layer of a complex forebody geometry. The main contributions of this paper are the analysis of the linear instability of the wake generated by a diamond-shaped roughness element immersed in a span-inhomogeneous base flow and the cross-validation of Navier-Stokes and spatial LST-2D simulations.

First, an isolated roughness was considered. The presence of the roughness in the span-inhomogeneous base flow leads to the formation of a crossflowlike vortex. Linear modal stability analysis was applied in the roughness wake, and three dominant high-frequency modes were identified. The roughness induces longitudinal streaks that are subject to a rapidly growing helical mode holding a single spiral. The second Mack mode present in the unperturbed boundary layer upstream of the roughness is also present in its wake, and its shape is strongly modulated by the roughness-induced stationary crossflow vortex. Finally, the secondary instability of the finite amplitude crossflow vortex was found to be the most unstable mode. The mode shapes and most amplified disturbance frequencies were found to be in good agreement with the most energetic spectral POD mode. The N-factor of the most unstable mode predicted by the LST-2D computations is also in close agreement with DNS predictions as it is only 10% lower.

The effect of a trip array configuration has also been investigated. The most unstable disturbances also consist of secondary instabilities located in the thin, inclined shear layer of the stationary crossflow vortices. The peak frequencies of these disturbances are higher than for the isolated roughness element.

Additional numerical investigations are needed to understand the effect of added freestream perturbations, of roughness height, and of trip-spacing ratio on the transition mechanisms. The use of PSE would be useful in taking nonparallel effects into account and improving the N-factor predictions compared to the LST-2D computations.

Acknowledgments

This work was funded by the Ministère des armées—Direction Générale de l'Armement/Defence Science and Technology Laboratory as part of the UK–France Ph.D. program. This work was performed using high-performance computing resources from grand équipement national de calcul intensif—Centre Informatique National de l'Enseignement Supérieur (GENCI-CINES) (Grant 2019-A0062A10738). The authors wish to gratefully thank T. André from MBDA-France for fruitful technical discussions.

References

- [1] Schneider, S. P., "Effects of Roughness on Hypersonic Boundary-Layer Transition," *Journal of Spacecraft and Rockets*, Vol. 45, No. 2, 2008, pp. 193–209.
<https://doi.org/10.2514/1.29713>
- [2] Lau, K., "Hypersonic Boundary-Layer Transition: Application to High-Speed Vehicle Design," *Journal of Spacecraft and Rockets*, Vol. 45, No. 2, 2008, pp. 176–183.
<https://doi.org/10.2514/1.31134>
- [3] Bartkowicz, M., Subbareddy, P., and Candler, G., "Numerical Simulations of Roughness Induced Instability in the Purdue Mach 6 Wind Tunnel," *40th Fluid Dynamics Conference and Exhibit*, AIAA Paper 2010-4723, 2010.
<https://doi.org/10.2514/6.2010-4723>
- [4] Paredes, P., Gosse, R., Theofilis, V., and Kimmel, R., "Linear Modal Instabilities of Hypersonic Flow over an Elliptic Cone," *Journal of Fluid Mechanics*, Vol. 804, Oct. 2016, pp. 442–466.
<https://doi.org/10.1017/jfm.2016.536>
- [5] Craig, S. A., and Saric, W. S., "Crossflow Instability in a Hypersonic Boundary Layer," *Journal of Fluid Mechanics*, Vol. 808, Dec. 2016, pp. 224–244.
<https://doi.org/10.1017/jfm.2016.643>
- [6] Ward, C. A. C., Henderson, R. O., and Schneider, S. P., "Possible Secondary Instability of Stationary Crossflow Vortices on an Inclined Cone at Mach 6," *45th AIAA Fluid Dynamics Conference*, AIAA Paper 2015-2773, 2015.
- [7] Moyes, A. J., Paredes, P., Kocian, T. S., and Reed, H. L., "Secondary Instability Analysis of Crossflow on a Hypersonic Yawed Straight Circular Cone," *Journal of Fluid Mechanics*, Vol. 812, Feb. 2017, pp. 370–397.
<https://doi.org/10.1017/jfm.2016.793>
- [8] Borg, M., Kimmel, R., and Stanfield, S., "Traveling Crossflow Instability for the HiFiRE-5 Elliptic Cone," *Journal of Spacecraft and Rockets*, Vol. 52, No. 3, 2015, pp. 664–673.
<https://doi.org/10.2514/1.A33145>
- [9] Li, F., Choudhari, M. M., and Duan, L., "Direct Numerical Simulation of Transition due to Traveling Crossflow Vortices," *45th AIAA Fluid Dynamics Conference*, AIAA Paper 2015-2771, 2015.
<https://doi.org/10.2514/6.2015-2771>
- [10] Shrestha, P., and Candler, G. V., "Direct Numerical Simulation of High-Speed Transition due to Roughness Elements," *Journal of Fluid Mechanics*, Vol. 868, June 2019, pp. 762–788.
<https://doi.org/10.1017/jfm.2019.179>
- [11] Choudhari, M. M., Li, F., Paredes, P., and Duan, L., "Computations of Crossflow Instability in Hypersonic Boundary Layers," *47th AIAA Fluid Dynamics Conference*, AIAA Paper 2017-4300, 2017.
<https://doi.org/10.2514/6.2017-4300>
- [12] Di Giovanni, A., and Stemmer, C., "Cross-Flow-Type Breakdown Induced by Distributed Roughness in the Boundary Layer of a Hypersonic Capsule Configuration," *Journal of Fluid Mechanics*, Vol. 856, Dec. 2018, pp. 470–503.
<https://doi.org/10.1017/jfm.2018.706>
- [13] Hein, S., Theiss, A., Di Giovanni, A., Schilden, T., Schröder, W., Paredes, P., Choudhari, M. M., Li, F., and Reshotko, E., "Numerical Investigation of Roughness Effects on Transition on Spherical Capsules," *Journal of Spacecraft and Rockets*, Vol. 56, No. 2, 2019, pp. 388–404.
<https://doi.org/10.2514/1.A34247>
- [14] Theiss, A., Hein, S., Ali, S. R. C., and Radespiel, R., "Wake Flow Instability Studies Behind Discrete Roughness Elements on a Generic Re-Entry Capsule," *46th AIAA Fluid Dynamics Conference*, AIAA Paper 2016-4382, 2016.
<https://doi.org/10.2514/6.2016-4382>
- [15] Li, F., Choudhari, M. M., Paredes, P., and Duan, L., "High-Frequency Instabilities of Stationary Crossflow Vortices in a Hypersonic Boundary Layer," *Physical Review Fluids*, Vol. 1, No. 5, 2016, pp. 1–32.
<https://doi.org/10.1103/PhysRevFluids.1.053603>
- [16] Choudhari, M. M., Li, F., Paredes, P., and Duan, L., "Nonlinear Evolution and Breakdown of Azimuthally Compact Crossflow Vortex Pattern over a Yawed Cone," *AIAA Aerospace Sciences Meeting*, AIAA Paper 2018-1823, 2018.
- [17] Durant, A., André, T., Edelman, J. B., Chynoweth, B. C., and Schneider, S. P., "Mach 6 Quiet Tunnel Laminar to Turbulent Investigation of a Generic Hypersonic Forebody," *20th AIAA International Space Planes and Hypersonic Systems and Technologies Conference*, AIAA Paper 2015-3575, 2015.
<https://doi.org/10.2514/6.2015-3575>
- [18] Orlik, E., Fedioun, I., and Davidenko, D., "Boundary-Layer Transition on a Hypersonic Forebody: Experiments and Calculations," *Journal of*

- Spacecraft and Rockets*, Vol. 48, No. 4, 2011, pp. 545–555.
<https://doi.org/10.2514/1.51570>
- [19] André, T., Durant, A., and Fedioun, I., “Numerical Study of Supersonic Boundary-Layer Transition due to Sonic Wall Injection,” *AIAA Journal*, Vol. 55, No. 5, 2017, pp. 1530–1547.
<https://doi.org/10.2514/1.J055164>
- [20] Cerminara, A., Durant, A., André, T., Sandham, N., and Taylor, N., “Receptivity to Freestream Acoustic Noise in Hypersonic Flow over a Generic Forebody,” *Journal of Spacecraft and Rockets*, Vol. 56, No. 2, 2019, pp. 447–457.
<https://doi.org/10.2514/1.A34283>
- [21] Reda, D. C., “Review and Synthesis of Roughness-Dominated Transition Correlations for Reentry Applications,” *Journal of Spacecraft and Rockets*, Vol. 39, No. 2, 2002, pp. 161–167.
<https://doi.org/10.2514/2.3803>
- [22] Cambier, L., Heib, S., and Plot, S., “The Onera elsA CFD Software: Input from Research and Feedback from Industry,” *Mechanics and Industry*, Vol. 14, No. 3, 2013, pp. 159–174.
<https://doi.org/10.1051/meca/2013056>
- [23] Liou, M.-S., “A Sequel to AUSM: AUSM⁺,” *Journal of Computational Physics*, Vol. 129, No. 2, 1996, pp. 364–382.
<https://doi.org/10.1006/jcph.1996.0256>
- [24] Lefieux, J., Garnier, E., and Sandham, N. D., “DNS Study of Roughness-Induced Transition at Mach 6,” *AIAA Aviation Forum*, AIAA Paper 2019-3082, 2019.
<https://doi.org/10.2514/6.2019-3082>
- [25] Blanc, F., “Patch Assembly: An Automated Overlapping Grid Assembly Strategy,” *Journal of Aircraft*, Vol. 47, No. 1, 2010, pp. 110–119.
<https://doi.org/10.2514/1.44116>
- [26] Mack, L., “Boundary-Layer Linear Stability Theory,” Special Course on Stability and Transition of Laminar Flows, AGARD Rept. 709, 1984.
- [27] Choudhari, M., Li, F., and Edwards, J., “Stability Analysis of Roughness Array Wake in a High-Speed Boundary Layer,” *47th AIAA Aerospace Sciences Meeting*, AIAA Paper 2009-0170, 2009.
<https://doi.org/10.2514/6.2009-170>
- [28] Montero, I. P., and Pinna, F., “BiGlobal Stability Analysis of the Wake Behind an Isolated Roughness Element in Hypersonic Flow,” *Proceedings of the Institution of Mechanical Engineers, Part G: Journal of Aerospace Engineering*, Vol. 234, No. 1, 2020, pp. 5–19.
<https://doi.org/10.1177/0954410019832733>
- [29] Brazier, J.-P., “Local Stability Analysis of a Round Jet Parallel to a Flat Plate,” *22nd AIAA/CEAS Aeroacoustics Conference*, AIAA Paper 2016-2733, 2016.
<https://doi.org/10.2514/6.2016-2733>
- [30] Lumley, J. L., *Stochastic Tools in Turbulence*, Academic Press, New York, 1970, Chap. 3.
- [31] Edelman, J. B., and Schneider, S. P., “Secondary Instabilities of Hypersonic Stationary Crossflow Waves,” *AIAA Journal*, Vol. 56, No. 1, 2017, pp. 1–11.
<https://doi.org/10.2514/1.J056028>
- [32] Xu, G., Chen, J., Liu, G., Dong, S., and Fu, S., “The Secondary Instabilities of Stationary Crossflow Vortices in a Mach 6 Swept Wing Flow,” *Journal of Fluid Mechanics*, Vol. 873, Aug. 2019, pp. 914–941.
<https://doi.org/10.1017/jfm.2019.397>
- [33] Mack, L. M., “On the Inviscid Acoustic-Mode Instability of Supersonic Shear Flows,” *Theoretical Computational Fluid Dynamics*, Vol. 2, No. 2, 1990, pp. 87–123.
<https://doi.org/10.1007/BF00272137>
- [34] De Tullio, N., and Sandham, N., “Influence of Boundary-Layer Disturbances on the Instability of a Roughness Wake in a High-Speed Boundary Layer,” *Journal of Fluid Mechanics*, Vol. 763, No. 10, 2015, pp. 136–165.
<https://doi.org/10.1017/jfm.2014.663>
- [35] Chen, X., Huang, G., and Lee, C., “Hypersonic Boundary Layer Transition on a Concave Wall: Stationary Görtler Vortices,” *Journal of Fluid Mechanics*, Vol. 865, April 2019, pp. 1–40.
<https://doi.org/10.1017/jfm.2019.24>
- [36] Li, F., Choudhari, M. M., and Paredes, P., “Nonlinear Görtler Vortices and Their Secondary Instability in a Hypersonic Boundary Layer,” *AIAA Aviation 2019 Forum*, AIAA Paper 2019-3216, 2019.
<https://doi.org/10.2514/6.2019-3216>
- [37] Choudhari, M. M., Li, F., and Paredes, P., “Streak Instabilities on HiFiRE-5 Elliptic Cone,” *AIAA Scitech 2020 Forum*, AIAA Paper 2020-0828, 2020.
<https://doi.org/10.2514/6.2020-0828>
- [38] Li, F., Choudhari, M., and Paredes, P., “Streak Instability Analysis for BOLT Configuration,” *AIAA Aviation 2020 Forum*, AIAA Paper 2020-3028, 2020.
<https://doi.org/10.2514/6.2020-3028>
- [39] De Tullio, N., Paredes, P., Sandham, N. D., and Theofilis, V., “Laminar-Turbulent Transition Induced by a Discrete Roughness Element in a Supersonic Boundary Layer,” *Journal of Fluid Mechanics*, Vol. 735, Nov. 2013, pp. 613–646.
<https://doi.org/10.1017/jfm.2013.520>
- [40] Whitehead, A. H., “Flowfield and Drag Characteristics of Several Boundary-Layer Tripping Elements in Hypersonic Flow,” NASA TND-5454, Oct. 1969.
- [41] Eckert, E. R. C., “Engineering Relations for Heat Transfer and Friction in High-Velocity Laminar and Turbulent Boundary Layer Flows over Surfaces with Constant Pressure and Temperature,” *Transactions of the ASME*, Vol. 78, No. 6, 1956, pp. 1273–1283.

J. Poggie
Associate Editor